INORGANIC CHEMISTRY FRONTIERS

RESEARCH ARTICLE

View Article Online
View Journal

Cite this: DOI: 10.1039/d5qi02196k

Symmetry control and magnetic exchange coupling in SMMs based on Co(II) complexes

Laura Cuevas-Contreras,[a] María Mar Quesada-Moreno,[b] Estibaliz Ruiz-Bilbao,[c] Juan Manuel Gutiérrez-Zorrilla,[c] J. Krzystek,[d] Mykhaylo Ozerov,[d] Juan-Ramón Jiménez *[a] and Enrique Colacio *[a]

This work reports on a mononuclear trigonal prismatic complex $[Co^{II}L](ClO_4)_2$ (**1**) and a trinuclear linear phenoxido-bridged complex $[(Co^{II}L1)_2Co^{II}]$ (**2**), where **L** and **H$_3$L1** are N_6 and N_3O_3 tripodal pro-ligands derived from the respective condensation of the *cis,cis*-1,3,5-tiaminocyclohexane with either 1-methyl-imidazol-2-carbaldehyde or salicylaldehyde. These compounds have been studied by X-ray single-crystal diffraction, dc and ac magnetism, High-Frequency and -Field Electron Paramagnetic Resonance spectroscopy (HFEPR), Far Infrared Magnetic Spectroscopy (FIRMS) and quantum chemical calculations. The results obtained for **1** show that N_6-tripodal Schiff-base ligands incorporating 1-methylimidazole donors yield trigonal-prismatic mononuclear complexes that typically display C_3 symmetry and exhibit very large, purely easy-axis magnetic anisotropy. In fact, complex **1** exhibits an energy gap between the ground and the first excited state ($2D$) of 228 cm^{-1} (directly measured by FIRMS), that can be considered the maximum limit for the easy-axis magnetic anisotropy in this type of complexes. The symmetry-driven large $2D$ value, together with the parallel alignment of the anisotropy axes, reduces QTM (Quantum Tunnelling of Magnetization) and yields mononuclear single-molecule magnet (MSMM) behaviour, with the observation of magnetic relaxation through a Raman process and open hysteresis at zero field. In compound **2**, the combination of the strong easy-axis anisotropy of the local Co^{II} ions, collinearity of the local anisotropy axes and sizable intramolecular magnetic exchange interactions between the Co^{II} ions in triple phenoxido-bridged linear trinuclear complexes causes the full quenching of the QTM and the observation of SMM behaviour with open hysteresis at zero field. Theoretical calculations point out that the magnetic interaction between the ground Kramers doublets (KDs) of the local Co^{II} ions generates four KDs and the magnetic relaxation occurs through the first excited KD *via* an Orbach process. Supporting this suggestion, the experimental value for the effective thermal energy barrier extracted from FIRMS of 76.8 cm^{-1} is not too far from the theoretical calculated value of 59.54 cm^{-1}.

Received 29th October 2025,
Accepted 31st January 2026

DOI: 10.1039/d5qi02196k

rsc.li/frontiers-inorganic

Introduction

Single molecule magnets (SMMs) are open-shell metal complexes exhibiting magnetic bistability at molecular level and blockade of the magnetization below the so-called blocking temperature (T_B).[1–9] As a consequence of this, these nanomagnets show slow relaxation of the magnetization and magnetic hysteresis. These systems have attracted a great deal of attention during the last decades, because they can show a fascinating combination of the above indicated classical properties and quantum properties, such as quantum tunnelling of the magnetization (QTM), quantum coherence and quantum oscillations.[10,11] These properties make them promising candidates for future applications in high-density information storage, quantum computing devices and molecular spintronics.[10–17] The SMM behaviour is usually tied to the existence of a thermal energy barrier (U_{eff}), which essentially depends on the magnetic anisotropy. This, in turn, is influenced by the combined action of spin–orbit coupling (SOC) and ligand field effects.[1–9] The first studies in this field were centred on polynuclear transition metal complexes. Later, the research interest moved toward lanthanide-based metal complexes because these metal ions possess large magnetic moment in the ground state and a strong SOC. These factors, together with the crystal field effects, can lead to sizeable magnetic anisotropy and

[a]*Departamento de Química Inorgánica, Facultad de Ciencias, Universidad de Granada, 18071 Granada, Spain. E-mail: ecolacio@ugr.es, jrjimenez@ugr.es*
[b]*Departamento de Química Física y Química Analítica, Universidad de Jaén, Campus Las Lagunillas, s/n, 23071 Jaén, Spain*
[c]*Departamento de Química Orgánica e Inorgánica, Facultad de Ciencia y Tecnología, Universidad del País Vasco UPV/EHU, P.O. Box 644, 48080 Bilbao, Spain*
[d]*National High Magnetic Field Laboratory, Florida State University, Tallahassee, Florida 32310, USA*

high-energy barrier for magnetization reversal (U_{eff}), specifically in the case of the Dy^{III} ion.[1–9,18] In recent years, research efforts in the field of SMMs have been focused on mononuclear lanthanide and transition metal complexes. This arises from the fact that in these simple magnets, called MSMMs (Mononuclear single-molecule magnets) or SIMs (Single-ion magnets), the magnetic anisotropy can be deliberately optimized by playing with the geometry and electronic nature of the metal ion and the crystal field spitting created by the ligands. The aim is to maximize the easy-axis magnetic anisotropy with a negligible rhombic term, which favours the SMM behaviour.[1–9,19–21] The most effective systems for this end are those with near-perfect axial symmetry, where the QTM that shortens spin lifetimes is almost fully suppressed. Following this crystal-field directed strategy, using large anisotropic Dy^{III} and Co^{II} ions and the tools provided by coordination chemistry, some important breakthroughs have been achieved. In particular, pseudo-two-coordinated Dy^{III}-metallocenes[22,23] and the Dy^{III} amide-alkene complex $[Dy\{N(Si^iPr_3)[Si(^iPr)_2C(CH_3)=CHCH_3]\}\{N(Si^iPr_3)(Si^iPr_2Et)\}]$ $[Al\{OC(CF_3)_3\}_4]$,[24] have shown U_{eff} and T_B values as high as 1843 cm^{-1} and 100 K, respectively, whereas two-coordinated Co^{II} based MSMMs have shown U_{eff} values of up to 450 cm^{-1}.[25] However, these systems are unstable to air and humidity, which is a serious restriction for technological applications. In view of this, highly stable Dy^{III} and Co^{II} based MSMMs with larger coordination numbers and easy-axis magnetic anisotropy in the ground state have been recently explored.[7,9,26–41] Among the latter systems, Co^{II} trigonal prismatic complexes with N_6-tripodal ligands and axial geometry occupy a prominent place because some of them show slow relaxation of the magnetization at zero field and pinched at the waist hysteresis loop.[31–33,38–44] Moreover, experimental and theoretical structure/anisotropy relationship studies on these compounds have demonstrated that the easy-axis anisotropy increases as the distortion from trigonal prismatic geometry (TPR-6) to octahedral (OC-6) decreases. This trend is accompanied by a parallel increase in the relaxation times.[45–48] In simpler terms, the MSMM properties improve when the geometry becomes closer to the ideal TPR-6. It is worth noting that the highest values of easy-axis magnetic anisotropy (determined directly by Far Infrared Magnetic Spectroscopy; FIRMS), of about $D = -115$ cm^{-1} with almost negligible E values (using the zero-field splitting formalism), were reported for three TPR-6 complexes. These systems were constructed using N_6-tripodal Schiff base ligands, where one of the triangular faces is made of three N donor atoms belonging to 1-methylimidazole moieties. Interestingly, two of these complexes[44] exhibit C_3 symmetry and thethird one quasi- C_3 symmetry,[42] which assures a strong easy-axis anisotropy with negligible transverse components and quenched QTM. It is noteworthy that in trigonal prismatic Co^{II} complexes, the magnetic relaxation generally does not take place over the large magnetic anisotropy barrier (U_{eff} = 2D if E = 0). Instead, the relaxation occurs through under-barrier processes, such as QTM and Raman, leading to relaxation times faster and T_B smaller than expected from the extracted U_{eff} values.[31–33,38–48] To achieve slow magnetic relaxation and, ideally, zero-field MSMM behaviour, the ground-state QTM must be minimized. This is typically accomplished by (i) enforcing near-perfect axial symmetry to suppress transverse anisotropy, (ii) reducing intermolecular dipolar coupling (*e.g.*, by magnetic dilution),[44,45,48,49] and (iii) eliminating hyperfine interactions *via* isotopes with zero nuclear spin.[50,51] In parallel, vibrational engineering is needed to weaken spin–phonon coupling and curb fast low-temperature Raman relaxation.[52–59]

For polynuclear complexes, QTM can also be suppressed by engineering strong exchange coupling between neighbouring metal centres, thereby enabling SMM behaviour.[7] This behaviour has been primarily observed for 3d–4f polynuclear SMMs with relatively strong ferro- or antiferromagnetic interactions between neighbouring 3d and 4f metal ions,[60–68] and for 4f-radical systems with very strong antiferromagnetic interactions between the spin carriers.[69,70] The interactions between 4f ions are usually very weak to suppress QTM, however, in some cases with carbon-based bridged ligands or metal–metal bonds in mixed-valence dilanthanide complexes, magnetic interactions are significantly enhanced, leading to hard or even ultra-hard SMM behaviour.[71–73] In this respect, it has been recently shown that the collinearity of the anisotropy axes and the strong 4f-radical Ising exchange interaction in the mixed-valence Ln^{III}–Ln^{II} dinuclear metallocene complex $[Dy_2I_3(CpiPr_5)_2]$, lead to a large separation of the ground and first excited states. This separation leads to the suppression of QTM and, as a result, to the up-to-date record of U_{eff} = 1631 cm^{-1} and T_B = 80 K.[73] The QTM suppression in transition metal clusters promoted by magnetic exchange interactions are limited to a few examples. Among them, two recently reported polynuclear Co^{II} complexes deserve to be highlighted. The first one is an air-stable linear Co^{II}-Radical-Co^{II} based SMM,[74] which was assembled from mononuclear tetrahedral Co^{II}-based MSMMs with strong easy-axis magnetic anisotropy. The strong magnetic exchange interaction between the spin carriers drastically slows down the magnetization relaxation, leading to hysteresis with a very small coercive field due to efficient quantum tunnelling. The second one is a trinuclear Co_3 which was recently reported by our group, where the large easy-axis anisotropy of both the external trigonal prismatic Co^{II} ions and the trigonal antiprismatic central Co^{II} ion, together with the collinearity of the anisotropy axes and magnetic exchange, leads to SMM behaviour at zero field with pinched at the waist hysteresis at 2 K.[75] It is worth noting that, to the best of our knowledge, this compound is the unique example of a Co_3 complex exhibiting open magnetic hysteresis at zero-field. It seems to be clear that the combination of strong local easy-axis anisotropies, collinearity of the anisotropy axes and magnetic exchange interactions are required to observe SMM in polynuclear linear complexes.

In this paper we report the synthesis, X-ray structures, magnetic properties, including HFEPR and FIRMS spectroscopies and theoretical calculations of the mononuclear trigonal prismatic complex $[Co^{II}L](ClO_4)_2$ and the trinuclear linear phenoxido-bridged complex $[(Co^{II}L1)_2Co^{II}]$, where **L** and **H_3L1** are N_6 and N_3O_3 tripodal pro-ligands derived from the condensation

of the *cis*,*cis*-1,3,5-tiaminocyclohexane with either 1-methylimidazol-2-carbaldehyde or salicylaldehyde, respectively (Scheme 1). The main aim of this work is fivefold: (i) to confirm that the use of 1-methylimidazole-2-carbaldehyde to construct N_6-tripodal Schiff bases favours the formation of mononuclear trigonal prismatic Co^{II} complexes with C_3 symmetry, approaching/reaching the limit of easy-axis magnetic anisotropy of this kind of complexes, (ii) to analyse if this strong anisotropy leads to MSMM behaviour at zero field, (iii) to demonstrate that N_3O_6 tripodal Schiff bases, obtained from tripodal triamines and salicylaldehyde, consistently yield linear trinuclear Co^{II} complexes with three μ-phenoxido bridges between the metal centres; in these complexes, the Co^{II} ions show strong easy-axis anisotropy, their local anisotropy axes are collinear, and there is substantial intramolecular exchange coupling, (iv) to support the hypothesis that the combination of these factors suppresses QTM allowing the observation of SMM behaviour at zero-field, and (v) to compare these complexes with previously reported analogues and, if possible, derive guidelines for improving their magnetic properties.

Experimental

General procedures

All reagents were obtained from commercial sources and used without further purification. The precursor *cis*,*cis*-cyclohexane-1,3,5-triamine trihydrobromide was prepared according to previously described procedures.[76,77]

Synthesis of the pro-ligand L

cis,*cis*-Cyclohexane-1,3,5-triamine trihydrobromide (0.3 g, 0.8 mmol) was added to a basic solution of NaOH (0.1 g, 2.4 mmol) in 1.5 mL of water. The mixture was stirred for 0.5 hours at room temperature, whereupon 1-methyl-2-imidazolecarboxaldehyde (0.3 g, 2.4 mmol) was added with continuous stirring. The resulting solution was refluxed for 1 hour, resulting in the formation of two phases. The organic layer was separated by using a decanting funnel, dried with anhydrous $MgSO_4$ and evaporated to dryness. Finally, a yellow oil was obtained. Yield: 42%. Anal. calc. for $C_{21}H_{27}C_9$: C, 62.20; H, 6.71; N, 31.09. Found: C, 62.23; H, 6.40; N, 31.36. ^{1}H NMR (400 MHz, DMSO-d_6, 298 K): 8.36 ppm (s, 3H, –CH═N–), 7.31 ppm (s, 3H, aromatic), 7.04 (s, 3H, aromatic), 3.93 ppm (m, 3H, –CH_3), 3.56 (m, 3H, ring –CH–N– ring), 1.81 ppm (m, 6H, ring –CH_2). TOF-MS-ES + (Da) (*m*/*z*): 406 $[M + H]^+$.

Synthesis of the pro-ligand H_3L1

This ligand was prepared using the same method as for ligand **L**, but using salicyl aldehyde instead of 1-methyl-2-imidazol-carboxaldehyde. Anal. calc. for $C_{27}H_{27}N_3O_3$: C, 73.45; H, 6.16; N, 9.52. Found: C, 72.81; H, 5.93; N, 9.45. ^{1}H-NMR (400 MHz, DMSO-d_6, 298 K):13.44 ppm (s, 3H, –OH), 8.67 ppm (s, 3H, –CH═N–), 7.45 (m, 3H, aromatic), 7.35 ppm (m, 3H, aromatic), 6.90 ppm (m, 6H, aromatic), 3.70 ppm (m, 3H, –CH–N– ring), 2.06 ppm (m, 3H, equatorial –CH_2 ring), 1.81(m, 3H, axial –CH_2 ring) TOF-MS-ES+ (Da) (*m*/*z*): 442 $[M + H]^+$.

In view of the ^{1}H RMN and TOF-MS-ES+ spectra and analytical results of these ligands, we decided to use them without further purification in the synthesis of the complexes.

Preparation of $[CoL](ClO_4)_2$ (1)

A solution of the pro-ligand **L** (0.4 g, 1 mmol) in 20 mL of methanol was added dropwise to a solution of $Co(ClO_4)_2{\cdot}6H_2O$ (0.4 g, 1 mmol) in 20 mL of methanol, whereupon an orange solid precipitated, which was filtered off, washed with methanol and air dried. Suitable crystals for X-ray diffraction were formed by slow diffusion of diethyl ether in a DMF solution containing the compound. The crystals were repeatedly washed with a 80/20 mixture of MeOH/CH_3CN and air-dried. Yield: 18%. Anal. calc. for $C_{21}H_{27}Cl_2CoN_9O_8$: C, 38.02; H, 4.10; N, 19.00. Found: C, 38.07; H, 4.25; N, 19.51. IR (cm^{-1}): 3100–2900, ν(C–H); 650–1630, ν(C═C and C═N); 1300, ν(C–N); 1080, ν(Cl–O) and 780, (CH).

Preparation of $[(CoL1)_2Co]{\cdot}2DMF$ (2) and $[(CoL1)_2Co]$ (2′)

The preparation of **2** was carried out under inert atmosphere using deoxygenated DMF as follows. A solution of $Co(OAc)_2$ (0.4 g, 1.6 mmol) in DMF (20 mL) was added dropwise to a

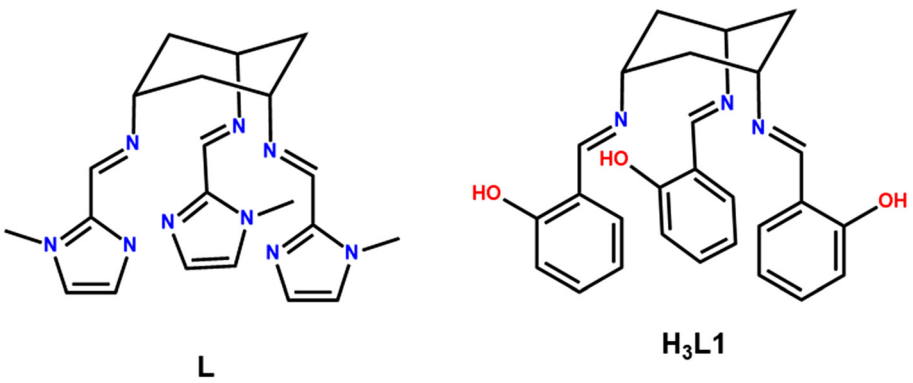

L H_3L1

Scheme 1 Structural formula of the pro-ligands L and H_3L1.

solution of the pro-ligand H_3L1(0.3 g, 0.8 mmol) in 20 mL of DMF. The resulting brown solution was kept under inert atmosphere for several days until the formation of red crystals suitable for X-ray diffraction. These crystals were filtered and repeatedly washed with an 80/20 mixture of $MeOH/CH_3CN$. When the crystals of **2** are removed from the solution, they lose the DMF solvent molecules leading to **2′**. Yield: 23%. Anal. calc. for $C_{54}H_{48}Co_3N_6O_6$: C, 61.55; H, 4.59; N, 7.98. Found: C, 61.18; H, 5.08; N, 7.76. IR (cm^{-1}): 2900, ν(C–H); 650–1630, ν(C=C and C=N); 1675–1615, ν(C–N); 1135, ν(C–O) and 740, (CH).

Physical measurements

Elemental analyses were performed on a Fisons-Carlo Erba analyser model EA 1108. IR spectra were recorded on a Bruker Tensor 27 spectrophotometer by using ATR detection. The X-ray powder diffraction (XRPD) spectra were recorded on a (2θ) Bruker D2-PHASER using CuKα (λ = 1.5418 Å) radiation and a LINXEYE detector, from 5 to 50° (2θ) at a scanning rate of 0.5°2θ min^{-1} (Fig. S1–S3). ^{1}H-RMN spectra were recorded at room temperature on a VARIAN DIRECT DRIVE (400 MHz) instrument using DMSO-d_6 as solvent (Fig. S4). TOF MS-ES+ mass spectra were recorded on Bruker Autoflex Speed in the linear ion mode (Fig. S5).

Variable-temperature (2–300 K) magnetic susceptibility measurements were carried out on polycrystalline samples under an applied field of 1000 Oe using a DynaCool PPMS-9 physical measurement equipment. Alternating-current (ac) susceptibility measurements under different applied static fields in the temperature range 2–20 K were performed in a PPMS-9 physical measurement equipment in the 50–10 000 Hz frequency range, using an oscillating field H_{ac} = 5 Oe. The magnetic susceptibility values were corrected for the diamagnetism of the molecular constituents and sample holder.

Far-infrared magnetic spectroscopy (FIRMS, also known as frequency-domain THz EPR spectroscopy)[78] experiments of the compounds were performed at the National High Magnetic Field Laboratory using a Bruker Vertex 80v FT-IR spectrometer coupled with a 17 T vertical-bore superconducting magnet in a Voigt configuration (light propagation perpendicular to the external magnetic field). The experimental setup employs broadband terahertz radiation emitted by a mercury arc lamp. The radiation transmitted through the sample was detected by a composite silicon bolometer (Infrared Laboratories) mounted at the end of the quasioptical transmission line. Both the sample and the bolometer were cooled by a low-pressure helium gas to the temperature of 5 K. The intensity spectra of the microcrystalline powder sample (~2 mg) bonded by n-eicosane were measured in the spectral region between 14 and 730 cm^{-1} (0.42–22 THz) with an instrumental resolution of 0.3 cm^{-1} (9 GHz). To discern the magnetic absorptions, the transmission spectrum at each magnetic field was divided by the reference spectrum, which is calculated as the average spectrum for all magnetic fields after removing outlier points at each frequency. Such normalised spectra are plotted as a heatmap and are sensitive only to subtle transmission changes induced by the magnetic field, while excluding strong non-magnetic contributions arising from vibrational absorption and instrumental response. All data analysis routines were implemented by in-house written MATLAB code based on the EPR simulation software package EasySpin.[79]

High-frequency and -field EPR (HFEPR) spectra were recorded at the National High Magnetic Field Laboratory in a 4.5–10 K temperature range on polycrystalline samples (20–25 mg), using a homodyne spectrometer at the EMR facility associated with a 15/17-T superconducting magnet and a frequency range from 52 to 426 GHz.[80] Detection was provided with an InSb hot electron bolometer (QMC Ltd, Cardiff, UK). The magnetic field was modulated at 50 kHz for detection purposes. A Stanford Research Systems SR830 lock-in amplifier converted the modulated signal to dc voltage.

Single-crystal structure determinations

Suitable crystals of **1** were mounted on a glass fibre and used for data collection. X-ray diffraction data were collected at 100 K using a Bruker D8 Venture diffractometer (MoKα radiation, λ = 0.71073 Å) outfitted with a PHOTON 100 detector. Unit-cell parameters were determined and refined on all observed reflections using APEX2 software.[81] Corrections for Lorentz polarisation and absorption were applied by SAINT[82] and SADABS[83] programs, respectively.

Intensity data for compounds **2** and **2′** were collected on an Agilent Technologies Supernova diffractometer equipped with monochromated (Mo-Kα radiation, λ = 0.71073 Å) and a HyPix (Hybrid Pixel Array) detector. Data frames (unit cell determination, intensity data integration and correction for Lorentz and polarisation effects) were carried out using CrysAlis Pro[84] software package.

The structures were solved using SHELXT[85] and refined by the full-matrix least-squares method on F^2 using SHELXL-2014/2018[86] and OLEX2 programs.[87]

A summary of selected data collection and refinement parameters for **1**, **2′** and **2** can be found in the SI (Tables S1–S3) and CCDC 2497812–2497814.

Computational methodology

Quantum-chemical calculations were carried out based on the crystallographic structures using the CIF files. The electronic structure and magnetic properties have been computed using state-averaged complete active space self-consistent field calculations (SA-CASSCF (7,5)),[88] followed by the N-electron valence second-order perturbation theory (NEVPT2) method[89–91] with the def2-TZVPP basis set,[92–94] including the auxiliary basis sets for correlation and Coulomb fitting for all the atoms. All calculations were performed with the ORCA 5.0.4 quantum chemistry program package.[95] Spin Hamiltonian parameters (D, E and g-tensor) were computed using the effective Hamiltonian S = 3/2. In this case, spin–orbit effects were included using the quasi-degenerate perturbation theory (QDPT).[96–100] The employed active space includes seven electrons in five 3d-orbitals of Co^{II} CAS (7,5). We have included all 10 states for the $2S + 1 = 4$ (quartet) states arising from the 4F and 4P terms of Co^{II}

and all the 40 states for the respective $2S + 1 = 2$ (duplet) states arising from the 2P, 2D (twice), 2F, 2G and 2H terms of the Co^{II} ion. ORCA produces two sets of results: CASSCF and NEVPT2. The splitting of d-orbitals due to ligand field has been computed with the *ab initio* ligand field theory (AILFT)[101] module implemented in ORCA program package.

Results and discussion

The tripodal compound *cis*,*cis*-1,3,5-cyclohexanetriamine (tach) has been previously used for designing N_6-tripodal Schiff base pro-ligands by reacting tach with different carbonyl compounds containing diazine moieties.[102–104] Some of these Schiff base tripodal pro-ligands were employed in preparing mononuclear trigonal prismatic Co^{II} complexes with strong easy axis magnetic anisotropy.[102–104] However, as far as we know, no examples of Co^{II} complexes prepared using **L** and **H_3L1** pro-ligands have been reported. The reaction of **L** with $Co(ClO_4)_2{\cdot}6H_2O$ in 1 : 1 molar ratio and using a methanol as solvent affords compound **1**, whereas H_3L1 reacts with Co $(OAc)_2{\cdot}4H_2O$ in a 2 : 3 molar ratio in the same mixture of solvents, leading to complex **2** in moderate yield. In this latter case, the acetate anion acts as a base to deprotonate the H_3L1 ligand. It is worth noting that using other Co^{II}/L molar ratios such as 1 : 2 or 2 : 1 and Co^{II}/H_3L1 ratios, such as 1 : 1 and 1 : 2, resulted only in the formation of compounds **1** and **2**, thus demonstrating their stability.

Crystals of compound **1** are stable in air at room temperature, but **2** easily loses solvent molecules leading to a single crystal-to-single crystal transformation (SCSC). Thus, when crystals of **2** are picked from the mother liquor and immediately measured, they belong to the $Ia\bar{3}d$ cubic space group. However, when crystals of **2** are allowed to stand at room temperature for two or three days, this compound loses the crystallisation solvent molecules and, even though the crystallinity is preserved, the crystals belong to the $P\bar{1}$ triclinic space group after this solid–solid transformation. The X-ray powder spectra for **2** and **2′** generated from the corresponding X-ray structures and those obtained from the experimental bulk compounds (Fig. S2 and S3) match well, thus demonstrating the purity of **2** and **2′**. As a consequence of this, we decided to use the desolvated compound (named **2′**) for magnetic and spectroscopic measurements.

X-ray crystal structures

Complex **1** crystallises in the trigonal space group $P3_1c$ and its structure consists of well-isolated cationic mononuclear $[Co^{II}L]^{2+}$ units whose charge is counterbalanced by the two perchlorate anions. Selected bond lengths and angles are given in Tables S4 and S5. Within the mononuclear cationic unit (Fig. 1), the cobalt atom is bonded to six nitrogen atoms belonging to the three arms of the ligand, giving rise to a CoN_6 coordination sphere.

The geometry of the CoN_6 coordination sphere was evaluated using the SHAPE program, which is based on the continuous shape measurements method (CShMs).[105] The extracted S(OC-6) and S(TPR-6) values of 10.184 and 1.198, respectively, indicate that the CoN_6 coordination polyhedron adopts a minimally distorted trigonal prismatic TPR-6 geometry (Table S6). In good agreement with this, the Bailar twist angle of 2.23° is very close to zero, the expected value for an ideal TPR-6 geometry. Moreover, the deviation with respect to the ideal Bailar pathway for the interchange between OC-6 (octahedral) and TPR-6 (trigonal prismatic) ideal geometries is very small (5.5%). In this description, the three nitrogen atoms from the imine groups occupy the vertices of one triangular face with bond distances of 2.162(2) Å, while the three nitrogen atoms belonging to the methyl-imidazole groups are in the vertices of the other triangular and parallel face with bond distances of 2.165(3) Å. The ratio between the mean donor-donor distance across a triangular face (s) of 2.963 Å and the mean donor-donor distances between the triangular faces (h) of 2.669 Å is s/h = 1.11, indicating a slightly compressed TPR-6 geometry (an ideal trigonal prism has nine edges of equal length and therefore s/h = 1). Moreover, the two trigonal

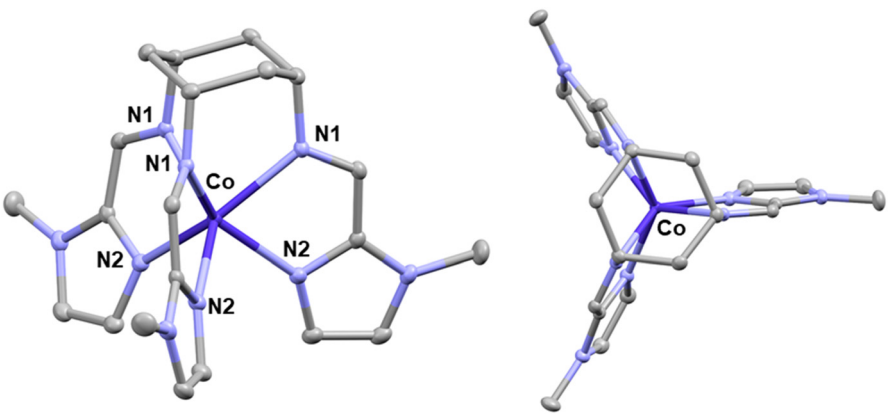

Fig. 1 ORTEP views of the molecular structure of **1** (left). View along the C_3 axis (right). Perchlorate anions are omitted for the sake of clarity. Atom's colour: N (light blue), Co (dark blue) and C (grey).

faces are strictly parallel and the distances between the coordinated imine nitrogen atoms across the triangular face (2.836 Å) are slightly shorter than the same distances across the face defined by the imidazole donor nitrogen atoms (3.089 Å), thus pointing to a small degree of truncation in the geometry (Fig. S6).

As a whole, the $[Co^{II}(L)]^{2+}$ units exhibit a strict C_3 symmetry, with the C_3 passing along the barycentre of the cyclohexane ring, the Co^{II} ion and the chloride atom of the perchlorate counteranion, and are involved in three weak $C_4H\cdots O_{perchlorate}$ interactions with the hydrogen bonded to the carbon atoms in the fourth position of the imidazole rings (Fig. S7). There is another C_3 axis passing through the chloride atom of the other perchlorate counteranion, which is involved in two $C_5H\cdots O$ interactions with two neighbouring $[Co^{II}(L)]^{2+}$ units. It is worth noting that all the C_3 axes in the structure of **1** are parallel. Finally, the shortest Co···Co intermolecular distance is 9.564 Å, showing that molecules are very well isolated in the structure (Fig. S8). There are small differences between the structure of **1** and those previously reported for other TPR-6 complexes constructed from N_6-tripodal Schiff base ligands, where one of the triangular faces, as in **1**, is formed by three N donor atoms belonging to the 1-methylimidazol moiety.[42–44] Such differences are: (i) the twist angle between triangular parallel faces is smaller for **1** (2.2° *vs.* ~9°), (ii) the six Co–N distances are almost equal in **1**, whereas in the related compounds the difference between the Co–$N_{imidazole}$ and the Co–N_{imine} bond distances is about 0.1 Å, (iii) the truncation of the TPR-6 geometry is somewhat larger in **1**, which could be the main reason for the slightly larger S(TPR-6) shape measures value for **1** (1.18 *vs.* 0.5). We believe that these tiny structural differences are not the decisive factors in determining the magnetic anisotropy and SMM behaviour of these compounds, but rather the existence of a C_3 axis and the parallel distribution of anisotropy axes in the structure (see below).

Complex **2′** crystallises in the triclinic $P\bar{1}$ space group (selected bond distances and angles are shown in Tables S7, S8 and S10, respectively, whereas Tables S11, S12 and S13 gather those corresponding to the parent compound **2**). The Co···Co intermolecular distances for both compounds are given in Table S9. The structure of **2′** consists of two very similar well-isolated linear trinuclear centrosymmetric Co^{II}_3 molecules (see Fig. 2), which have a pseudo-C_3 axis along the Co–Co–Co direction and the centre of symmetry located at the central Co^{II} ion (namely Co(2)). Within these centrosymmetric molecules, two fully deprotonated tripodal ligands ($L1^{3-}$) are bonded to the Co^{II} peripheral ions (namely Co(1)) through the imine nitrogen and the phenoxide oxygen atoms, affording a CoN_3O_3 coordination sphere. The phenoxide oxygen atoms of the two $L1^{3-}$ coordinated ligands are additionally linked at opposite sides of the central Co(2) ion, giving rise to perfect linear Co_3 molecules where Co(2) and Co(1) ions are connected by triple phenoxide bridging groups, resulting in a CoO_6 coordination sphere for the Co(2) ion. Mean Co(1)–N and Co(1)–O distances are found in the 2.136–2.151 Å and 2.106–2.122 Å ranges, respectively, whereas the Co(2)–O distances are between 2.083 Å and 2.126 Å. Both bond distances are typical of Co^{II} complexes with this kind of donor atoms. Continuous shape measures using the SHAPE software[105] (see Table S10) indicate that the coordination sphere of the Co(1) ions is very close to the ideal TPR-6 polyhedron (STPR6 = 1.235 and 1.669 for molecules A and B, respectively) with a small deviation from the Bailar TPR6 ↔ OC-6 deformation pathway (% path deviation of 4.7 and 4.9 for molecules A and B, respectively). In good agreement with the small distortion of the TPR-6 geometry of the Co(1) coordination polyhedron, the mean Bailar angles are 12.4°. The triangular faces determined by the imine nitrogen atoms and the phenoxide oxygen atoms are virtually parallel (mean angle value between the planes of 0.5°) with mean N···N and O···O distances across the faces of 2.965 Å and 2.573 Å, respectively, which indicates a significant truncation of the trigonal prismatic geometry (Fig. S9). Conversely, the $Co(2)O_6$ coordination sphere is closer to a perfect octahedral geometry (SOC-6 = 2.643 and 2.768 for

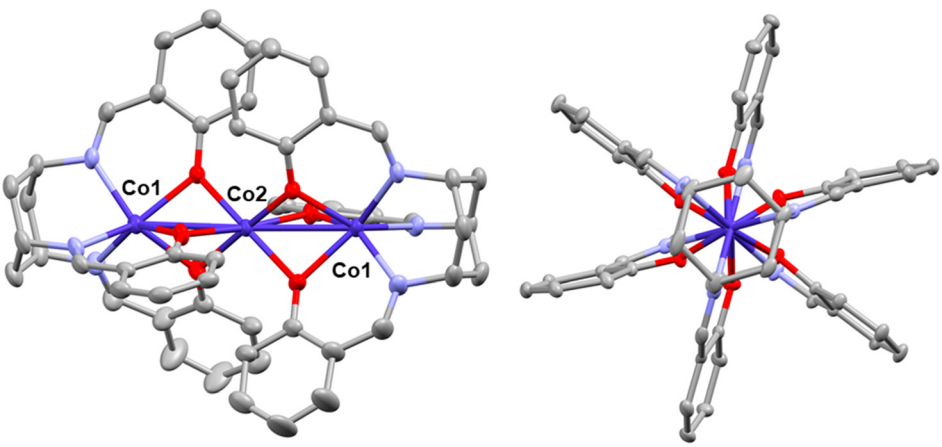

Fig. 2 ORTEP views of the molecular structure of **2′**. View along the pseudo C_3 axis showing the paddle-wheel arrangement of the ligands (right). Atom's colour: N (light blue), Co (dark blue), O (red) and C (grey).

molecules A and B, respectively) with a significant elongation along the C_3 axis: the mean s/h ratio defined as the mean donor–donor distance across the triangular faces divided by the donor–donor distances between the triangular parallel faces is 0.78, and the α angle between the pseudo-C_3 and Co–O directions is 45.3° (Fig. S9), which are less than 1.0 and 54.74°, the values of s/h and α for the non-elongated octahedron, respectively. The steric hindrance between the arms of the two coordinated ligands causes them to rotate by 60° relative to each other, giving rise to a paddle-wheel arrangement of the ligands when the molecule is viewed along the pseudo-C_3 intermetallic axis (Fig. 2, right), which is characteristic of linear trinuclear complexes.[75,106,107] Consequently, the CoO_6 coordination sphere can be viewed as a trigonal antiprism elongated along the pseudo-C_3 axis.

The mean shortest intramolecular Co(1)···Co(2) and Co(1)···Co(1) distances are 2.977 Å and 5.954 Å, respectively, whereas the shortest intermolecular distances of 6.916 Å and 7.114 Å correspond to Co(1)···Co(1) distances between two neighbouring molecules of A and B, respectively (Fig. S10). The pseudo-C_3 axis of molecules A and B are not parallel but form an angle of 60.13°.

The main differences between **2′** and the related complex [{Co(μ-L′)}$_2$Co] (where L′ = 1,1,1-tris[(salicylideneamino) methyl]ethane)[68] are: (i) the CoN_3O_6 coordination environment of the external Co(II) ions is closer to an ideal TPR-geometry in the former than in the latter, (ii) the Co(2) central ion, however, is slightly more distorted from the ideal OC-6 geometry in compound **2′**, (iii) the Co(1)···Co(1) and Co(1)···Co(2) distances are both slightly larger in **2′** and, consequently, the Co(1)–O–Co(1) bridging angles (mean value of 90.1° for the former and 88.3° for the latter), (iv) the θ angle between the N_3 and O_3 triangular parallel faces is larger for the former (12.42°) than for the latter (9.7°), whereas the mean ϕ angles between the Co(1)–O–Co(2) plane and the plane of the phenyl ring is larger for the latter than for the former.

It should be noted at this point that the structure of **2** is very similar to that of **2′**, with very close bond distances and angles. A brief description of this structure is given in the SI.

Magnetic properties

The temperature dependence of the magnetic properties of polycrystalline samples of complexes **1** and **2′** in the 2–300 K temperature range was measured under an applied magnetic field of 0.1 T and is given in the form $\chi_M T$ *vs.* T (χ_M being the molar magnetic susceptibility) in Fig. 3. At room temperature, the $\chi_M T$ value for **1** of 3.25 cm^3 mol^{-1} K is much higher than the spin-only value (1.875 cm^3 mol^{-1} K) for one isolated isotropic Co^{II} ion with g = 2 and S = 3/2, which indicates the existence of unquenched orbital angular momentum of the Co^{II} ion. On lowering the temperature, the $\chi_M T$ product first remains almost constant from room temperature to about 150 K and then steadily decreases to reach a minimum value of 2.58 cm^3 mol^{-1} K at 2 K. This behaviour is mostly due to the depopulation of the Kramers doublets arising from the spin–orbit coupling (SOC) effects, which are responsible for magnetic anisotropy.

The field dependence of the magnetisation of **1** in the 3–6 K temperature range and magnetic fields ranging from 0 to 7 T is represented in the inset of Fig. 3. The magnetisation value at 3 K under the maximum applied field of 7 T of 2.37Nμ_B is much smaller than the theoretical saturation value of 3Nμ_B expected for an isolated Co^{II} ion with g = 2 and S = 3/2. This fact corroborates the existence of significant magnetic anisotropy in this complex.[19] The M *vs.* H/T isotherms for **1** (Fig. S11) virtually superimpose on a single master curve, thus suggesting that the energy separation between the ground and first excited Kramers doublets could be very large for this compound.[19]

The results of the theoretical *ab initio* calculations for **1** (see SI) suggest that the zero-field splitting (ZFS) Spin Hamiltonian (eqn (1)) would be appropriate for analysing the magnetic properties of **1**. Therefore, the magnetic susceptibility and magnetisation data for **1** were simultaneous fitted with the following Hamiltonian, using the PHI program.[108]

$$\hat{\boldsymbol{H}} = D\left[\hat{\boldsymbol{S}}_z^2 - S(S+1)/3\right] + E\left(\hat{\boldsymbol{S}}_x^2 - \hat{\boldsymbol{S}}_y^2\right) + \mu_B \sum_{i=x,y,z} g_i \vec{H}_i \hat{\boldsymbol{S}}_i \quad (1)$$

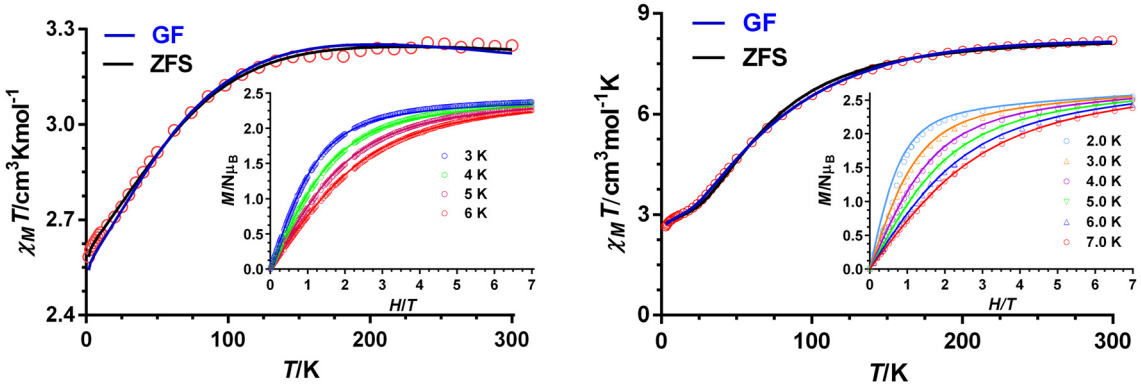

Fig. 3 Temperature dependence of $\chi_M T$ and field dependence of the magnetization (inset) for **1** (left) and **2′** (right). The solid lines represent the best fit with the Hamiltonians given in eqn (1) and (2) for **1** and eqn (3) and (4) for **2′**.

where the first and second terms are ZFS terms that account for the axial magnetic anisotropy and the rhombic magnetic anisotropy, respectively, and the third term represents the Zeeman interaction (μ_B is the Bohr magneton, H the applied magnetic field, and g is the anisotropic g-tensor). The best-fitting procedure with $g_x = g_y$ afforded the following ZFS parameters: D = −108.1 (2) cm^{-1}, E = −0.08 (1) cm^{-1}, $g_x = g_y$ = 2.2883 (4) and g_z = 3.0367 (2), $R = 1.6 \times 10^{-6}$. The energy gap between the two low-lying Kramers doublets $\Delta E_1 = E(\mathrm{KD1}) - E(\mathrm{KD2})$ is 216.2 cm^{-1}. It should be mentioned that the intrinsic limitations of this phenomenological approach, together with the inaccuracy of the dc magnetic measurements for determining the ZFS parameters, specifically E and $|E/D|$, prevent reliable extraction of the sign of D and the magnitude of E from dc magnetic data. In any case, the D value obtained from dc magnetic measurements should be considered with caution and supported by theoretical and other experimental techniques. Despite this, the ZFS Hamiltonian has been widely applied for evaluating the magnetic anisotropy in trigonal prismatic Co^{II} complexes (see Table S14).[31–33,38–48]

Compound **1** exhibits a trigonal prismatic geometry and first-order SOC, so that a Hamiltonian that considers the SOC, like the Griffith-Figgis Hamiltonian (GF),[109–111] could probably be more appropriate than the ZFS approach. The GF model takes advantage of the T–P isomorphism that considers that the real orbital angular momentum for the $^4T_{1g}$ ground state in an ideal O_h geometry is equal to the orbital angular momentum of the ^4P free ion term (L_{eff} = 1) multiplied by −3/2. However, for trigonal prismatic complexes, the lowest crystal-field terms arise from the ^4E ground term and, therefore, the use of the GF Hamiltonian is doubtful. With this limitation in mind, the magnetic susceptibility and magnetisation data for **1** were also simultaneously fitted with the GF phenomenological Hamiltonian:

$$\hat{H} = -\sigma\hat{\boldsymbol{L}}\hat{\boldsymbol{S}} + \sigma^2 B_2^0\left(3\hat{L}_z{}^2 - \hat{\boldsymbol{L}}^2\right) + \frac{B_2^2}{2}\sigma^2\left(\hat{L}_x{}^2 - \hat{L}_y{}^2\right) + \mu_B\left[-\sigma\hat{\boldsymbol{L}}_u + g_e\hat{\boldsymbol{S}}_u\right]\vec{H}_u \quad (u = x, y, z). \tag{2}$$

The first term accounts for the interaction between the spin (S = 3/2) and orbital (L = 1) angular moments through the spin–orbit coupling, where λ represents the spin–orbit coupling constant. The parameter σ represents a combined reduction factor, which comprises the isomorphism coefficient (−3/2) and the orbital-reduction parameter (κ) (σ varies from −3/2 for weak ligand field to −1 for a strong ligand field). The second and third terms describe the effect of the axial and rhombic crystal fields (B_2^0 and B_2^2 are the crystal field parameters). The best fit parameters for compound **1** using the GF Hamiltonian and by including a term accounting for the temperature-independent paramagnetism (TIP) were B_2^0 = −316 cm^{-1}, B_2^2 = −0.05 cm^{-1}, σ = −1.64, λ = −127, TIP = 0.42 × 10^{-3} and $R = 3.6 \times 10^{-6}$. The energy gap between the two low-lying Kramers doublets $\Delta E_1 = E(\mathrm{KD1}) - E(\mathrm{KD2})$ is 203.1 cm^{-1}, very close to that extracted using the ZFS model. The Δ_{axial} and $\Delta_{rhombic}$ derived from the crystal field parameters are 2550 cm^{-1} and 0.001 cm^{-1}, respectively (Δ_{axial} and $\Delta_{rhombic}$ represent the splitting of the crystal ground term due to the axial and rhombic components of the crystal field).[110] The large value of the former parameter and the negligible value for the latter support the very large easy-axis magnetic anisotropy of compound **1**. It should be mentioned that even though the fit is rather good (see Fig. 3), it is worse than that obtained with the ZFS model, and moreover, the σ value is abnormally high, thus suggesting that for trigonal complexes with a C_3 axis and very large easy-axis magnetic anisotropy, the GF model does not seem to be the most appropriate choice. In view of the above considerations, the magnetic anisotropy parameters extracted from ZFS and GF Hamiltonians should be taken with caution, as none of them could be fully suitable for analysing the magnetic properties of **1**. Regardless of the model, compound **1** exhibits a huge easy-axis anisotropy, as can be expected for quasi-ideal trigonal prismatic complexes with a C_3 symmetry axis (see Table S14)

The low-lying spin–orbit energy levels extracted from the fitting of the magnetic data and those calculated by CASSCF/NEVPT2 (see below the theoretical calculations section) are given in Fig. 4.

For comparative purposes, we have collected in Table S14 some magneto-structural information concerning hexacoordinate Co^{II}-MSMMs with geometry closer to TPR-6 than to OC-6. The data in this table confirm that when the geometry becomes nearer to the ideal TPR6 (that is to say, when the continuous shape measure S_{TPR6} is closer to zero), the easy-axis magnetic anisotropy increases (larger negative values of D or Δ_{axial} and lower values of E and $\Delta_{rhombic}$) and the MSMM properties improve. In this regard, it is not surprising that MSMMs at the upper part of the table (close to ideal TPR-6 geometry) show not only slow relaxation at zero field but, in most cases, pinched at the waist magnetic hysteresis at 2 K. Nevertheless, only in three instances, including **1**, the hysteresis is open at H_{dc} = 0. In the lower part of the table, when E or $\Delta_{rhombic}$ increases and E/D (or $\Delta_{rhombic}/\Delta_{axial}$) is greater than approximately 0.15, the QTM arising from the transversal an-

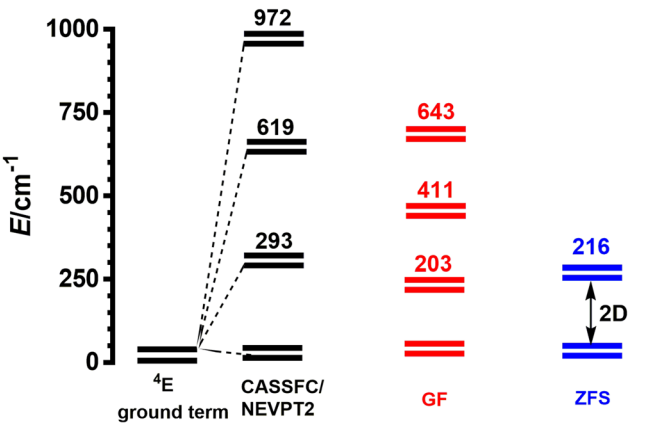

Fig. 4 Low-lying spin–orbit energy levels for **1** extracted from theoretical calculations and magnetic data.

isotropy prevents the compounds from exhibiting SMR at zero-field and they become field-induced MSMMs with no hysteresis at 2 K.

Regarding compound **2′**, the room temperature $\chi_M T$ value of 8.19 $cm^3\ mol^{-1}$ K is much higher than the expected spin-only value (5.625 $cm^3\ mol^{-1}$ K) for three non-interacting isotropic Co^{II} ions with $g = 2$ and $S = 3/2$, which, like in **1**, points to an unquenched orbital contribution of the Co^{II} ions (Fig. 3 right). As the temperature is lowered from room temperature, the $\chi_M T$ product decreases first slightly from room temperature to 150 K and then in a sharper manner to reach a quasi-plateau of 2.65 $cm^3\ mol^{-1}$ K around 15 K. This decrease is largely due to sizeable antiferromagnetic interactions between the Co^{II} ions through the triple phenoxido bridges and to the depopulation of the Kramers doublets arising from the SOC effects.[75] The field dependence of the magnetization up to 7 T in the temperature range 2–7 K is shown in Fig. 3 (inset). The value of the magnetization at 7 T and 2 K ($2.55N\mu_B$) is much lower than the saturation value expected for a system with three isolated octahedral Co^{II} ions with $S = 3/2$ and $g = 2$ ($\approx 6.3N\mu_B$), but it is not far from the value expected for an isolated Co^{II} ion ($\approx 2.1N\mu_B$), arising from the intratrinuclear antiferromagnetic coupling between the three Co^{II} ions.

The magnetic data were analysed using the following anisotropic spin-Hamiltonian:

$$\hat{H} = -J\left(\hat{\boldsymbol{S}}_1\hat{\boldsymbol{S}}_2 + \hat{\boldsymbol{S}}_2\hat{\boldsymbol{S}}_3\right) - J\left(\hat{\boldsymbol{S}}_1\hat{\boldsymbol{S}}_3\right) + \sum_{i=1}^{3}\left[D\left(\hat{\boldsymbol{S}}_{zi}{}^2 - S(S+1)/3\right) + E\left(\hat{\boldsymbol{S}}_x{}^2 - \hat{\boldsymbol{S}}_y{}^2\right) + \beta\vec{H}g\hat{\boldsymbol{S}}_i\right] \quad (3)$$

where the first and second terms account for the intramolecular magnetic couplings, the third and fourth ones correspond to the single ion axial magnetic anisotropy and the rhombic magnetic anisotropy, respectively, and finally the fifth term represents the Zeeman interaction. The susceptibility and magnetisation data were simultaneously fitted using the PHI software[108] with the above Hamiltonian. To avoid overparameterisation and due to the low accuracy of dc data in determining the magnitude of E, this parameter was fixed to zero. J' is expected to be very weak and then was also fixed to zero. Moreover, an axial g matrix with $g_x = g_y$ was considered, and the same D, g_z and g_{xy} values were assumed for the three Co^{II} ions. A good quality fit was obtained with the following parameters: $J = -10.14(3)$ cm^{-1}, $g_z = 3.110(3)$, $g_{xy} = 2.005(9)$, $D = -68.5(9)$ cm^{-1} and $R = 6.5 \times 10^{-4}$. It is worth mentioning that by imposing positive D values, the resulting fit was of much worse quality with large residual errors. It should also be indicated that similar residual errors were obtained for negative D values between −50 and −100 cm^{-1}. When both J and J' were allowed to vary freely, the fit showed that these parameters were correlated, and this provided an additional reason to fix J' to zero in the fitting procedure.

The Co(1) and Co(2) ions in **2′** exhibit distorted trigonal prismatic and trigonal antiprismatic coordination spheres, respectively, and therefore must possess significant unquenched orbital angular momentum.[66] In view of this, the magnetic data were also analysed with the following anisotropic Hamiltonian that considers the existence of first-order SOC. The Hamiltonian used for analysing the magnetic data is given in eqn (2).

$$\boldsymbol{H} = -J\left(\hat{\boldsymbol{S}}_1\hat{\boldsymbol{S}}_2 + \hat{\boldsymbol{S}}_2\hat{\boldsymbol{S}}_3\right) - J'\left(\hat{\boldsymbol{S}}_1\hat{\boldsymbol{S}}_3\right) + \sum_{i=1}^{3}\left[-\sigma\lambda\hat{\boldsymbol{L}}\hat{\boldsymbol{S}} + \Delta_{ax}\left(\hat{\boldsymbol{L}}_z{}^2 - \frac{2}{3}\right) + \Delta_{rh}\left(\hat{\boldsymbol{L}}_x{}^2 - \hat{\boldsymbol{L}}_y{}^2\right) + \beta\left[-\sigma\hat{\boldsymbol{L}}_u + g_e\hat{\boldsymbol{S}}_u\right]\hat{H}_u\right] \quad (4)$$

where $u = x, y, z$, Δ_{ax} and Δ_{rh} represent the splitting of the crystal ground term due to the axial and rhombic distortion of the crystal field. The rest of parameters have their usual meaning (see above eqn (2) and (3)). To avoid overparameterisation of the data, J' and Δ_{rh} were fixed to zero, as both parameters should be very small, almost negligible. Moreover, an average σ value was assumed for the three Co^{II} ions. The axial parameters for the external and central Co^{II} ions were named Δ_{13} and Δ_2, respectively. A very good quality fit was obtained with $J = -9.60$ (2) cm^{-1}, $\lambda = 132(1)$ cm^{-1}, $\sigma = -1.38(2)$, $\Delta_{13} = -1776(4)$ cm^{-1} ($B_2^0 = 310.9$ cm^{-1}) and $\Delta_2 = -679$ (2) cm^{-1} ($B_2^2 = 118.8$ cm^{-1}) (see Fig. 3). The negative values extracted for the parameters Δ_{13} and Δ_2 point out the strong easy-axis magnetic anisotropy of the Co(II) ions in **2′**, in line with the results extracted with the spin Hamiltonian (eqn (3)).

It is worth noting that, as far as we know, the correlation between the sign and magnitude of the magnetic exchange interaction and structural parameters is still not well established for phenoxido-bridged polynuclear Co^{II} complexes. This is because, among other reasons, high-spin Co^{II} complexes are generally subjected to SOC (orbital angular momentum is not quenched), and moreover, they have four interacting magnetic orbitals involving several ferromagnetic (F) and antiferromagnetic (AF) magnetic exchange pathways. These factors in turn depend on the structural and geometrical parameters of the specific complex. Owing to this, it is not possible, in most of the cases, to predict with guarantee the sign and magnitude of the magnetic interaction in these types of complexes. A recent experimental study carried out on bis(phenoxido)-bridged dinuclear Co^{II} complexes[112] has shown that the interaction is generally AF and, in a few cases F, this latter occurring when the Co–O–Co angle in the bridging region is smaller than 99.7° and the dihedral angle between the Co–$(O)_2$–Co plane and the phenyl plane (δ) is larger than 35°. However, diphenoxido- or triphenoxido-bridged trinuclear Co^{II} complexes with Co–O–Co as small as 90°, like those observed for **2′**, present AF interactions.[75,113] In some cases, a slight change in the Co–O–Co angle of about 1° switches the magnetic interaction from AF to F.[113] In spite of these inconsistent results, it is generally accepted that larger Co–O–Co angles and smaller dihedral angles (δ) favour AF interactions. Taking into account these considerations, compound **2′** with a larger Co–O–Co angle and a smaller δ angle than the related [{Co(μ-L′)}$_2$Co] complex (where L2 = 1,1,1-tris[(salicylideneamino)methyl] ethane)[75] should exhibit a somewhat larger intramolecular

magnetic exchange coupling, which is in agreement with the results derived from dc magnetic measurements.

Theoretical calculations

Complexes **1** and **2′** have been studied by multiconfigurational *ab initio* calculations (CASSCF/NEVPT2) using the experimental X-ray structural data and the ORCA 5.0.4 program package[95] (see Tables S15–S21, SI). It should be noted that in the case of **1**, calculations with and without perchlorate anions yielded almost identical results, and therefore only the results for the $[Co(L)]^{2+}$ cationic unit are hereafter discussed. The calculated spin-free states energies (Table S15) for **1** indicate that the two lowest spin quartet states are virtually degenerate (the gap of 0.2 cm^{-1} between them can be considered an intrinsic error of the computational method), as expected for compounds with C_3 symmetry, leading to a ^4E term. For this kind of pseudotrigonal prismatic Co^{II} complexes, $\langle Lz \rangle$ is larger than 1.5, and then the first-order SOC is operative,[65,66] leading to the splitting of the ^4E term into four almost equidistant KDs,[65,66] with an energy gap between them of about 300 cm^{-1} (Table S16). The energy gap between the ground and the second excited KDs is 618.8 cm^{-1}, so that the latter will remain scarcely populated (~5%). In these circumstances the effective ZFS spin Hamiltonian (eqn (1)) could be suitable to phenomenologically analyse the theoretical results. The results extracted using this approach with the SINGLE_ANISO module[114,115] point out, as expected for trigonal prismatic Co^{II} complexes with C_3 symmetry, that: (i) compound **1** presents strong axial easy-axis magnetic anisotropy with a large negative D value of −146.4 cm^{-1} and a very small E/D parameter of 0.013 (actually, C_3 symmetry requires the absence of rhombic anisotropy, so E should be zero) and (ii) the computed g-tensor components for the $S = 3/2$ manifold, or alternatively the effective g' values for the lowest KD, are consistent with almost negligible rhombic anisotropy (Table 1), with the anisotropy axis aligned along the C_3 axis of the cationic $[Co^{II}(L1)]^{2+}$ unit.[25,42–44]

The splitting of the d orbitals for **1**, calculated using the *ab initio* ligand field theory method (AILFT) implemented in ORCA, together with the electronic configuration corresponding to the ^4E ground term are represented in Fig. 5, respectively, whereas their energies and one electron wavefunctions are given in Table S17.

Table 1 Computed ZFS parameters D, E, $|E/D|$ and g values for the ground state of compound **1**. δE_1 and ΔE_1 are the calculated first excitation energies before and after considering spin–orbit effects, respectively

Compound	Method	D (cm^{-1})	E/D	E (cm^{-1})	δE_1 (cm^{-1})	ΔE_1 (cm^{-1})	g_x, g_y, g_z[a], g'_x, g'_y, g'_z[b]
1	CASSCF	−142.638[c]	0.016375[c]	−2.336[c]	0.2	285.39	1.31, 1.34, 3.48[a] 0.11, 0.11, 9.70[b]
	CASSCF/NEVPT2	−146.446[c]	0.012899[c]	−1.889[c]	0.2	292.96	1.29, 1.31, 3.48[a] 0.08, 0.08, 9.70[b]

[a] g-Tensor for the true spin $S = 3/2$. [b] Effective g'-tensors assuming a pseudospin $S = 1/2$. [c] Obtained using the single_aniso module.

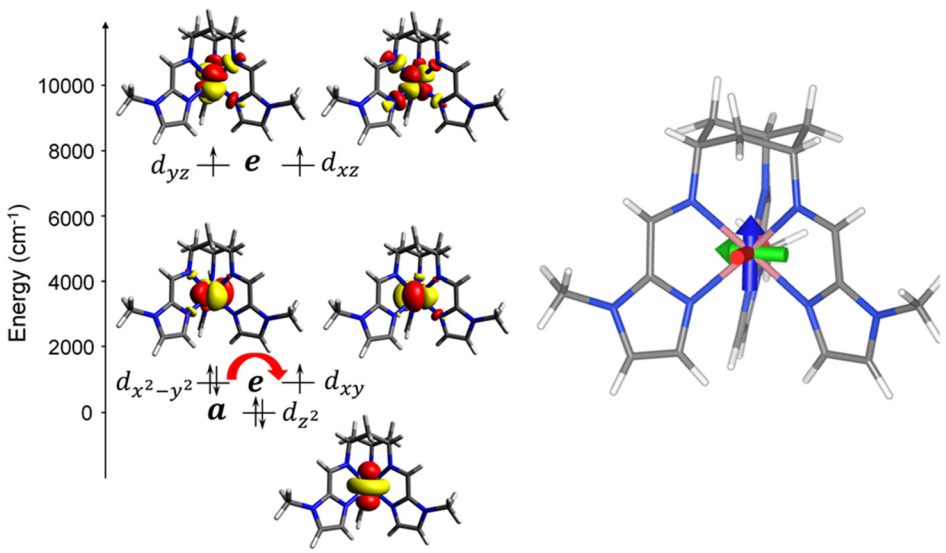

Fig. 5 (Left) NEVPT2-AILFT computed d-orbital energy diagram of **1**. (Right) Orientation of the g-tensor components obtained from CASSCF/NEVPT2 calculations. The reference axis x, y and z of the g-tensor are displayed in red, green and blue, respectively. Counterions and solvent molecules are omitted for clarity. The length of the arrows does not represent the magnitude of the g-tensor components but only the orientation.

The sign and magnitude of D can be qualitatively predicted from the spin-allowed part of the second-order perturbative treatment,[116] which depends on the inverse of the excitation energies. Since the first excitation energy involves the transfer of a single electron from the last doubly occupied orbital ($d_{x^2-y^2}$) to the first semi-occupied orbital (d_{xy}), which are almost degenerate and have the same m_l value (±2), a large negative D value can be expected. This result agrees well in sign and magnitude with the theoretical value extracted from the ZFS Hamiltonian (see above). It is worth noting at this point that the electronic structure and the values of the D, E and g_i parameters for this compound are very similar to those previously extracted by our group for structurally related complexes with N_6-tripodal ligands with C_3 symmetry.[42,45,48]

In the case of **2′**, to calculate the electronic structure of each mononuclear Co^{II} fragment in the trinuclear Co_3 unit, two of the Co^{II} ions were replaced by Zn^{II} ions. The energies extracted for the spin-free states (ligand field terms) of Co(1) and Co(2) ions (Table S18) indicate that the energy gap between the ground and first excited states is of 133.5 cm^{-1} and 222.6 cm^{-1}, respectively, and therefore, in both cases, the lowest two spin quartet states are close to degeneracy. This fact suggests a small Jahn–Teller effect and the existence of first-order SOC for both types of Co^{II} ions. However, the second excited state for both types of Co^{II} ions is above 6000 cm^{-1} and 2000 cm^{-1} for Co(1) for Co(2), respectively. As a result of the first order SOC, as in the case of compound **1**, four almost equidistant KDs are obtained, with an energy gap between the ground and first excited KDs at the NEVPT2 level of 282.53 and 233.11 cm^{-1} for Co(1) and Co(2), respectively (Table S19). Since the second excited KD for Co(1) and Co(2), is located at ∼ 635 and ∼596 cm^{-1} above the ground state, respectively, it will be barely populated (∼ 6%) and, consequently, an effective zero-field splitting (ZFS) spin Hamiltonian (eqn (1)) could be appropriate to analyse the theoretical results for each Co^{II} fragment.

The calculated D and E values using this Hamiltonian are given in Table 2 together with the effective g values (g_{eff}) for each doublet projected on a S = 1/2 pseudospin. The large and negative D values for Co(1) and Co(2) indicate their strong easy-axis anisotropy, as expected for Co^{II} ions with trigonal prismatic and trigonal antiprismatic geometries, respectively. It is worth noting that the easy-axis anisotropy is stronger for Co(1), whereas the rhombicity (E/D) is larger for Co(2). The effective g values for both Co^{II} ions support the easy-axis anisotropy of the ground state and the larger rhombicity for Co(2). The anisotropy axes for Co(1) and Co(2) are located along the pseudo-C_3 axis passing through the Co(1)–Co(2)–Co(1) direction (Fig. S12).

It should be noted that the largest negative contribution to D for Co(1) and Co(2) arises from the first excited quartet state, $^4\Phi_1$ (see Table S20), which is the closest in energy to the ground quartet state. The splitting of the d orbitals for Co(1) and Co(2) (Fig. S13 and Table S21), calculated as indicated above for compound **1**, points out that the first excitation energy involves the transfer of a single electron from the last doubly-occupied orbital (d_{xy}) to the first semi-occupied orbital ($d_{x^2-y^2}$) for Co(1) and *vice versa* for Co(2). Both orbitals have the same m_l value (±2) and are separated by a small energy of 153 cm^{-1} and 108 cm^{-1} for Co(1) and Co(2), respectively, so that large negative D values are expected (see above for **1**). This result matches well in sign and magnitude with the theoretical values calculated using the ZFS Hamiltonian.

To support the easy-axis magnetic anisotropy of this compound and to directly determine the magnitude of the energy gap between the ground and first excited state (≈2D), we have performed FIRMS (Far-InfraRed Magnetic Spectroscopy) and HFEPR (High-Frequency and -Field Electron Paramagnetic Spectroscopy).

HFEPR and FIRMS spectroscopies

The HFEPR spectrum of **1** (Fig. S14) shows a weak resonance at 4.5 K in the frequency range 237–408 GHz located at g_{eff} ∼9.1. This resonance can only be assigned to the parallel turning point ($B\|z$) of the intra-Kramers transition from M_S $|-3/2\rangle$ to $|+3/2\rangle$ within the ±3/2 ground manifold and it has been previously observed in the HFEPR spectra of other Co^{II} complexes with a trigonal prismatic coordination sphere and large easy-axis anisotropy, like **1**, with g_{zeff} values in the 7–9 range.[45,48,117,118] The perpendicular turning points of the same transition ($B\|$ x, y) could appear well outside the upper limit of the accessible magnetic field (17 T) and therefore were not observed. The transition from Ms = $|-3/2\rangle$ to $|+3/2\rangle$ is forbidden, because it corresponds to ΔM_s = ±3 (only transitions with ΔM_S = ±1 are allowed), but it appears because the selection rule is relaxed in the presence of the E-term in the spin Hamiltonian, which mixes the $|\pm3/2\rangle$ and $|\pm1/2\rangle$ Kramers doublets. The larger the E value, the more allowed the $|-3/2\rangle$

Table 2 Computed ZFS parameters D, E, $|E/D|$ and g values for the ground state of the Co^{II} ions in **2′**. Co(1) and Co(2) refer to the respective edge and middle Co^{II} ions. δE_1 and ΔE_1 are the calculated first excitation energies before and after considering spin–orbit effects, respectively

Co(II) ion	Method	D (cm^{-1})	E/D	E (cm^{-1})	δE_1 (cm^{-1})	ΔE_1 (cm^{-1})	g_x, g_y, g_z[a] g'_x, g'_y, g'_z[b]
Co(1)	CASSCF/NEVPT2	−129.639	0.052933	−6.862	87.8	260.37	1.51, 1.58, 3.34[a] 0.35, 0.35, 9.35[b]
Co(2)	CASSCF/NEVPT2	−116.222	0.180246	−20.949	115.4	243.51	1.57, 1.80, 3.25[a] 1.16, 1.24, 8.86[b]

[a] g-Tensor for the true spin S = 3/2. [b] Effective g'-tensors assuming a pseudospin S = 1/2.

to $|+3/2\rangle$ transition becomes. In the case of **1**, the weakness of the observed resonance indicates that E is very small with an estimated $E/D \approx 0.03$.[119] This result is in good agreement with the *ab initio* E/D value of 0.013 (see Table 1). Since only a single and weak EPR resonance could be observed, corresponding to the $B\|z$ turning point of the intra-Kramers transition within the $M_s = \pm 3/2$ multiplet, no information on the ZFS parameters D or E could be extracted. To determine these parameters, it is necessary to observe inter-Kramers transitions. The only result reported in this manuscript is $g_z(\text{eff}) = \sim 9.1$ For an axial-anisotropy $S = 3/2$ spin state, $g_z(\text{eff})$ is approximately equal to $3 \times g_z(\text{intrinsic})$,[117] so $g_z(\text{intrinsic})$ is about 3.0. This is corroborated by both magnetometry and calculations.

The FIRMS heat map of **1** is shown in Fig. 6 along with the transmission spectra for 0 and 17.5 Tesla. This heat map displays the effect of the magnetic field on transmission. Two broad dips at 234 and 252 cm^{-1} correspond to phonon absorption, which exhibits an extremely weak shift with the applied magnetic field due to spin–phonon coupling. This subtle shift gives rise to the nearly vertical features in the heatmap, with interruptions where the strongly field-dependent magnetic resonance modes intersect the phonons. Although these distortions are present, the most intense change at zero field occurs at 227.4 cm^{-1}, corresponding to a narrow dip clearly observed in the transmission spectra. This feature becomes smeared with increasing magnetic field, while the broad dips remain essentially unaffected.

Based on the pattern observed in the FIRMS map, we infer that the feature at 227 cm^{-1} is the ZFS peak, which in turn corresponds to the $2D^*$ value (the energy gap between the ground and first excited KD in an $S = 3/2$ system). This $2D^*$ value is of the same order of magnitude as those extracted from fitting the magnetic data and from theoretical calculations for **1** using the ZFS model, as well as those reported for other Co^{II}-SIMs with C_3 symmetry and very large easy-axis anisotropy.[42–44] All these compounds present $2D^*$ values close to 225 cm^{-1} and can therefore be considered as the upper limit of easy-axis magnetic anisotropy for trigonal prismatic Co^{II} complexes.

Interestingly, the FIRMS spectrum of compound **2′** shows a weak but detectable magnetic transition at 76.8 cm^{-1} (Fig. S15). The energy of this magnetic transition is not too far from the energy gap between the ground and first excited states calculated for the exchange-coupled system (see below, Fig. 9). The HFEPR of **2′** is silent in the frequency range *ca.* 100–600 GHz at cryogenic temperatures (5–10 K), as observed for the related trinuclear complex previously reported by our group.[75] The lack of resonances could be tentatively explained using the theoretically calculated exchange energy spectrum of this compound (Fig. 9), extracted using the POLY_ANISO module[120] in ORCA software package. From the ground state Kramers doublet for each Co^{II} atom in **2′** (calculated with the SINGLE_ANISO module), four Kramers doublets are obtained. Each of these KDs is built from $\Delta M_s = \pm 3/2$ KDs of the local Co^{II} ions, and therefore the intra-Kramers doublet transition for the ground $\Delta M_s = \pm 3/2$ KD and the inter-Kramers transitions of the coupled system are forbidden. Moreover, the first excited state is also a $\Delta M_s = \pm 3/2$ KD that lies outside the energy range accessible at the applied frequencies.

Dynamic properties

To know if compounds **1** and **2′** exhibit slow magnetic relaxation and SMM/SIM behaviour at zero field, their dynamic of the magnetisation was examined by performing temperature and frequency dependence studies of the ac magnetic susceptibility under a 5 Oe alternating field on polycrystalline samples of the compounds. Both compounds exhibit temperature- and

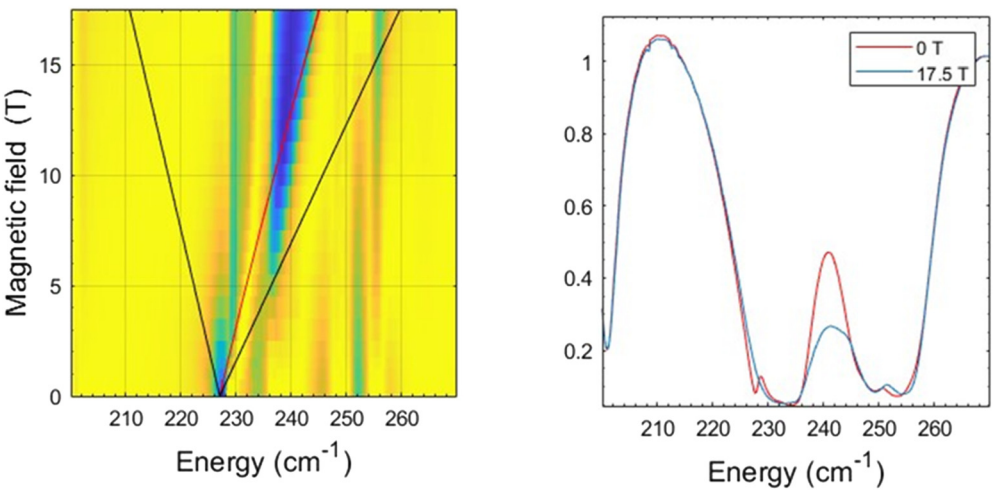

Fig. 6 (Left) Experimental 2-D (magnetic field *vs.* energy) heat maps of FIRMS response of complex **1**. Regions marked in blue represent resonance absorption that is sensitive to changing magnetic field. Regions in yellow are insensitive to the field. The most intense change is observed at 227.4 cm^{-1} in zero field. The lines are simulations of turning points for the spin Hamiltonian, using a $S = 3/2$ and the extracted spin Hamiltonian parameters. (Right) Transmission spectra recorded on a powder pellet of the complex at $T = 4.2$ K and at the indicated magnetic fields.

frequency-dependent ac susceptibility peaks at zero field. In the case of **1**, the temperature dependence of the out-of-phase ac susceptibility (χ''_M) at different frequencies (Fig. S16) shows signals below 28 K with no clear maxima in the 10–16 K range due to the existence of fast quantum tunnelling of magnetisation (QTM),[44,48] which is responsible for the rise in χ''_M observed below 10 K. QTM can arise from the existence of weak dipolar interactions,[44,45,48,49] hyperfine interactions with the Co^{II} nuclear spin (I = 7/2) and transverse anisotropy. In addition, a distortion of the structure at low temperature could also provoke the appearance of transverse anisotropy. Calculations with the SINGLE_ANISO code implemented in the ORCA 5.0.4 program package, which neither considers the two former interactions nor the distortion of the structure, indicate that QTM in the ground state could be at least partly discarded in **1**. This is because the computed transverse magnetic moment for the QTM transition is $0.028\mu_B$ (Fig. S17), which is close to, but smaller than the generally assumed value of 0.1 needed for an efficient relaxation mechanism.[116] Moreover, in good agreement with this, calculations also show that compound **1** has a very small transverse magnetic anisotropy (E/D = 0.013).

From the frequency dependence of χ''_M below 16 K and using the generalised Debye model, the temperature dependence of the relaxation times was extracted. The τ *vs.* $1/T$ data appeared to follow an Arrhenius-like relaxation regime in the high-temperature region that becomes temperature independent below about 8 K because of QTM (Fig. 7). The thermally activated energy barrier (U_{eff}) extracted from the linear region of the curve at high temperatures is 38(5) K. This value is by far lower than $|2D^*|$ (energy gap between the ground and first excited states) values extracted from *ab initio* calculations, dc static magnetic measurements and FIRMS results ($|2D|\sim220$ cm^{-1}). Therefore, the thermally activated Orbach relaxation process, which takes place through real states, can be discarded from eqn (5), which represents some of the possible mechanisms that can contribute to the magnetic relaxation

$$\tau^{-1} = AT + {\tau_{QTM}}^{-1} + CT^n + \tau_0 \exp\left(-\frac{U_{eff}}{k_B T}\right) \quad (5)$$

In this equation, the first two terms represent the field-dependent direct and QTM relaxation processes, respectively, whereas the third and fourth terms describe the field-independent Raman and Orbach relaxation processes. Because the direct process (first term in the equation) is not active at zero field, the τ^{-1} *vs.* T data for **1** were fitted to a combination of Raman and QTM (third and second terms in eqn (5), respectively). The best fit parameters were A = 0.01(1) s^{-1} K^{-n}, n = 5.5(4) and τ_{QTM} = 0.00004(1) s^{-1}. The α values extracted from the Cole–Cole plot for **1** at zero field (Fig. S18) in the 8–17 K region are found in the 0.11–0.37 range and the curves do not show the semicircular shape typical of a single relaxation process. These results are in good agreement with the contribution of Raman and QTM processes to the magnetisation relaxation. The former operates in the whole temperature range, while QTM dominates at very low temperatures (below 8 K).

As indicated elsewhere, the observation of magnetisation relaxation in slightly distorted trigonal prismatic Co^{II} complexes like **1** at zero applied magnetic field is rather unusual. On the basis of the results for **1** and other similar complexes[42–44] we can hypothesise that zero-field magnetic relaxation is mainly due to the following structural factors that do not favour the appearance of QTM: (i) the small distortion of the TPR-6 geometry due to the C_3 symmetry, leading to a perfect axial anisotropy (E = 0) representing the upper limit of easy-axis magnetic anisotropy for trigonal prismatic Co^{II} complexes, (ii) the relatively long Co···Co distances (>9.5 Å) leading to very small, if any, intermolecular magnetic interactions, and (iii) the magnetic anisotropy axes of the ground Kramers doublets corresponding to neighbouring molecules with the shortest Co···Co distances are all parallel.[121–123]

Finally, it should be noted that, despite the above indicated factors favouring the elimination of QTM, this process is still observed for **1**, which could be mainly due to hyperfine interactions, opening up new avenues for magnetic relaxation, and/or to a distortion of the molecule at low temperature that lowers the symmetry from C_3 and induces significant transversal anisotropy. Moreover, strong spin–phonon coupling for some thermally populated vibrational modes could also con-

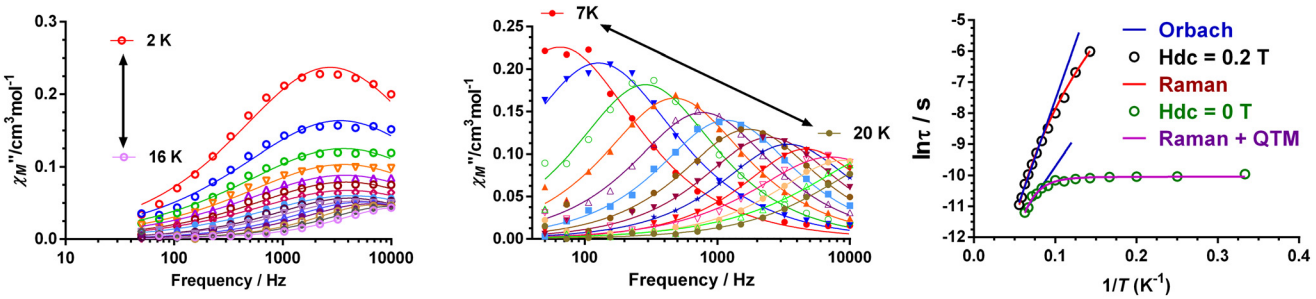

Fig. 7 (Left) Frequency dependence of the χ''_M at the indicated temperatures under H_{dc} = 0 (left), and H_{dc} = 2000 Oe (middle). (Right) Temperature dependence of the relaxation time τ in the form $\ln\tau$ *vs.* $1/T$. The solid lines represent the best fits of the experimental data: a combination of Raman and QTM processes (purple line), a Raman process (red line) and the blue lines correspond to the fit of the linear high temperature data to the Orbach process.

tribute to the fast Raman relaxation operating at low temperature.[52,54,124]

To try to eliminate the QTM in complex **1**, ac measurements were performed in the presence of small dc fields (500–2500 Oe). From the field and frequency dependence data of χ''_M at 10 K, the optimal magnetic field for the ac measurements (promoting the slowest relaxation) was determined to be 2000 Oe (Fig. S19). A complete set of temperature- and frequency-dependent ac susceptibility measurements were then carried out at the optimal field below 26 K (Fig. 7, middle). Now, the temperature dependence of the out-of-phase ac susceptibility (χ''_M) at different frequencies (Fig. S20) shows clear maxima in the 18 K (10 000 Hz)–7 K(100 Hz) range. From the χ''_M *vs.* frequency data and using the generalised Debye model, the temperature dependence of the relaxation time at 2000 Oe was extracted for **1**, which is given in the form ln τ *vs.* 1/T in Fig. 7 (right panel). The high-temperature region of this plot obeys the Arrhenius law with U_{eff} and τ_0 values of 74(3) K and 3.02(4) × 10^{-7} s, respectively. This U_{eff} value at 0.2 T is higher than that extracted from the data at zero field, but it is still much lower than the experimental and calculated $|2D^*|$ values of ~220 cm^{-1}. In view of this, the Orbach process can be ruled out, and then the 1/τ *vs.* T data were fitted only to a Raman process, leading to the following best parameters: C = 0.014(2) s^{-1} K^{-n} and n = 5.3 (3). The field dependence of the relaxation time (Fig. S15) shows an almost constant value for H > 1500 Oe, thus indicating an almost negligible contribution of the direct process (since it depends on H^4, the relaxation time is expected to decrease as the magnetic field increases). If, in addition to the Raman, the contribution of the direct process (first term of eqn (5)) is taken into account, the resulting fit is of similar quality and the following best-fit parameters can be extracted: A = 54 (2) s^{-1} K^{-1}, C = 0.008 (1) s^{-1} K^{-n} and n = 5.4 (3). These parameters indicate that the contribution of the direct relaxation mechanism is very small compared to the Raman process. It should be noted that the values of the C and n parameters connected with the Raman relaxation process are close to those obtained from the data at zero-field. Although a n value of 9 would be expected for Kramers ions,[125] smaller n values can be considered as acceptable depending on the structure of the levels, and if both acoustic and optical phonons are considered.[126,127] It should be noted at this point that, under the optimal field, the QTM is not fully quenched, as evidenced by a very small rising tail observed below 5 K (Fig. S20). In view of this, and to try to fully eliminate QTM, we decided to measure several magnetically diluted versions of **1** with Co/Zn = 1/10 and 1/5 molar ratios, but all attempts were unsuccessful.

The Cole–Cole plot for **1** (Fig. S21) in the 9–17 K region presents small α values ranging from 0.02 to 0.07 and the curves show a semicircular shape, thus indicating that a single relaxation process (Raman process) is operative. However, below 8 K, the α values increase until reaching values of 0.13 at 7 K, due to the small QTM contribution at very low temperature.

Regarding compound **2′**, ac measurements show frequency-dependent peaks in the 4.5–9.5 K temperature range under zero magnetic field (Fig. 8). From these data and using the generalised Deby model, the temperature dependence of the relaxation time was extracted and represented in the form ln τ *vs.* 1/T in Fig. 8 (right). Interestingly, the experimental points do not deviate from linearity, thus indicating that they obey the Arrhenius law, typical of an over-barrier thermally activated Orbach process. In agreement with the existence of only this relaxation process, the temperature dependence of the out-of-phase ac magnetic susceptibility at different frequencies (Fig. S22) does not exhibit any sign of QTM and the Cole–Cole plots are semicircular (Fig. S23) with small α values in the 0.08 (4 K)–0.18 (10 K) range. In view of the above considerations, the temperature dependence of the relaxation time was fitted to the equation for an Orbach process, leading to the following parameters: τ_0 = 4.63 (2) × 10^{-8} s and U_{eff} = 53(0) K. It is worth noting that the extracted U_{eff} value is much smaller than the computed energy barriers for the local Co^{II} ions (above 230 cm^{-1}), thus suggesting that either the magnetic relaxation

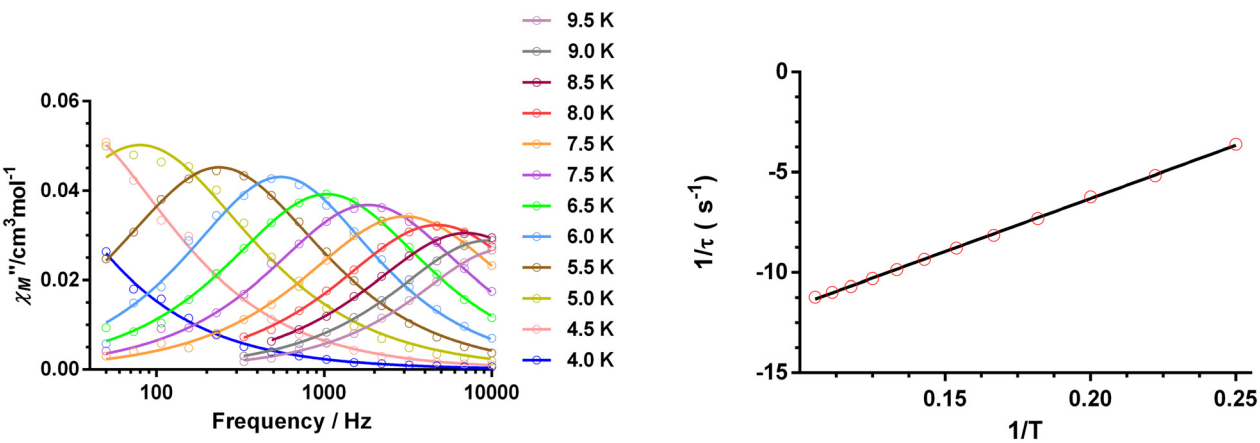

Fig. 8 (Left) Frequency dependence of the χ''_M at the indicated temperatures under H_{dc} = 0. The solid lines represent the best fits of the experimental data to the generalized Debye model (Right) Temperature dependence of the relaxation time τ in the form ln τ *vs.* 1/T. The solid black line represents the best fit of the experimental data to a Orbach process.

takes place through a Raman process arising from the individual metal ions, like in **1**, or comes from a thermally activated Orbach process tied to the energy level structure of the magnetic exchange coupled system.

To disclose the origin of the experimental magnetic relaxation, we have calculated the electronic structure of the Co(1) and Co(2) ions and their blocking barriers using the SINGLE_ANISO code[114,115] implemented in the ORCA program package (see Fig. S24). As observed in this figure, the matrix element of the transverse magnetic moment in the ground state of Co(2) is of $0.32\mu_B$, larger than the generally assumed value of 0.1 necessary for an efficient relaxation mechanism *via* QTM within this state and, therefore, slow magnetic relaxation arising from Co(2) is unlikely to be operative.[116] However, the corresponding matrix element of Co(1) is smaller than this threshold value and therefore QTM could be quenched. Nevertheless, it could be promoted by hyperfine and intermolecular interactions. If QTM was quenched and the magnetic relaxation was single-ion in origin, it could occur through Raman process involving virtual excited states, probably due to coupling between vibrational modes of the molecule and phonons. The fact that the experimental points of the $\ln \tau$ *vs.* $1/T$ plot do not deviate from a straight line (see above), points out that the single-ion Raman process could also be discarded and so the relaxation process must occur through an Orbach process arising from the magnetic exchange coupled Co_3 complex. To support this hypothesis, we carried out calculations for the magnetic exchange-coupled system using the POLY_ANISO code[120] also implemented in ORCA. This program applies the Lines model[128] to fit the experimental susceptibility data, using the theoretically calculated energies and wave functions of the ground doublets of the individual Co(1) and Co(2) ions extracted with the SINGLE_ANISO code. In this case, the Lines model is entirely appropriate because both Co^{II} ions have strong axiality of the ground KD. The effective isotropic exchange Hamiltonian employed to analyse the data is as follows:

$$H_{exch} = -J(\hat{S}_1\hat{S}_2 + \hat{S}_2\hat{S}_3) - J'(\hat{S}_1\hat{S}_3) \quad (6)$$

The best fit of the magnetic susceptibility data, obtained by fixing $J' = 0$ led to the magnetic exchange parameters $J = -14.00\ cm^{-1}$ and $zJ = -0.375\ cm^{-1}$ (Fig. S21). The zJ parameter had to be included in the Hamiltonian (eqn (6)) to consider the diminution of $\chi_M T$ at very low temperature, which must be mainly due to intermolecular interactions. It is worth mentioning that the fit of the susceptibility data considering $J' = -0.5\ cm^{-1}$ and the same values of $J = -14.00\ cm^{-1}$ and $zJ = -0.375\ cm^{-1}$ does not noticeably change the quality of the fitting and the value of J (see Fig. S25). However, when zJ is not considered, the J value does not change but the quality of the fit becomes poorer (Fig. S26). From the extracted magnetic parameters, the energy levels spectrum of the magnetic exchange-coupled Co_3 system was calculated, as shown in Fig. 9 (right). The spectrum involves four KD doublets (eight states) arising from the Kramers ground state of each Co(II) site ($2 \times 2 \times 2 = 8$). These KDs are grouped according to the values of their magnetic moments, which reach a maximum along the pseudo-trigonal C_3 axis. As can be observed in Fig. 9, the magnetic moment matrix element for the ground state exchange KD doublet is very small ($0.11 \times 10^{-3}\mu_B$) and hence QTM within the ground state is expected to be quenched, which matches well with the fact that **2'** exhibits slow magnetic relaxation at $H_{dc} = 0$. However, a thermal-assisted QTM relaxation *via* the first or second excited states at 59.54 cm^{-1}, which are degenerate (the gap between them in Fig. 9 is shown for

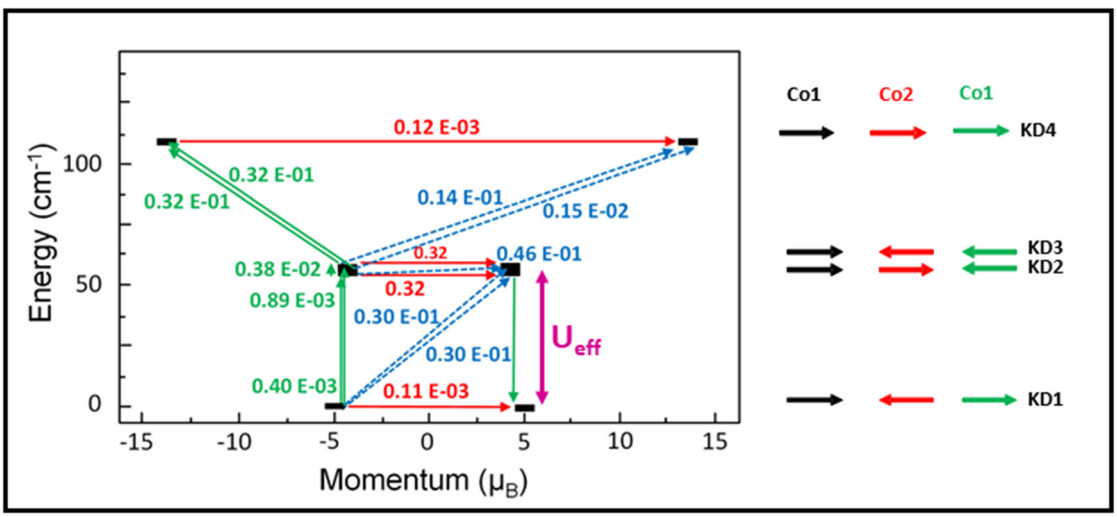

Fig. 9 (Left) The *ab initio* POLY-ANISO computed magnetisation blocking barrier for **2'**. The thick black lines represent the four lowest exchange KDs as a function of their magnetic moment along the main anisotropy axis. Green lines indicate the magnetisation reversal mechanism. Red lines correspond to QTM and thermally assisted QTM (TA-QTM). Blue dashed lines represent the possible Orbach mechanism. The values close to the arrows indicate the matrix elements of the transition magnetic moments. (Right) Internal magnetic structure of the four exchange KDs.

illustrative purposes), could be possible as the matrix element for this relaxation pathway is $0.32\mu_B$. The calculated U_{eff} value for the relaxation through the first excited state of 59.54 cm^{-1} is not too far from the U_{eff} values of 36.8 cm^{-1} and 76.8 cm^{-1} extracted from the temperature dependence of the relaxation times and FIRMs (see above), respectively. The difference between the experimental and theoretically estimated thermal energy barriers can be due to limitations inherent to the theoretical method and possible relaxation involving a vibrationally excited state of the electronic ground state.[52,54,124] The fact that the U_{eff} value for **2′** is stronger than that for the related complex $[\{Co(\mu\text{-}L')\}_2Co]$[75] must be a result of the larger J value extracted for the former, pushing the excited state to a higher energy.

To verify the SMM behaviour of **1** and **2′** we carried out magnetisation hysteresis loop measurements on a powdered sample with a sweep-rate of 100 Oe s^{-1} in the 2–3 K temperature range (Fig. 10). Butterfly-shaped hysteresis loops are observed for these complexes at 2 K with small openings at zero-field, which indicate the occurrence of SMM behaviour with effective QTM. The coercive field and remnant magnetisation values are $0.07\mu_B$ and 210 Oe for **1** and $0.22\mu_B$ and 1400 Oe for **2′**. Compound **1** exhibits worse hysteresis parameters at zero field than **2′**, which is in good agreement with the existence of a smaller QTM contribution for the latter due the largely eliminated QTM by magnetic exchange coupling. It should be noted that at 3 K no appreciable hysteresis loop was observed at 100 Oe s^{-1} for these compounds. Although the hysteresis loop measurements for the previously reported complex $[\{Co(\mu\text{-}L')\}_2Co]$[75] were performed at a sweep-rate of 50 Oe s^{-1}, the hysteresis parameters for this compound seem to be worse than those extracted for **2′**, which is in accordance with the stronger U_{eff} energy barrier extracted for this latter compound. It is worth mentioning that the presence of open hysteresis above 2 K at zero field in homometallic polynuclear Co^{II}-based SMMs is quite infrequent.[25,74,75]

Although several examples of trinuclear Co^{II} complexes have been reported so far, only three of them exhibit slow magnetic relaxation at zero field above 2 K: $[\{Co(\mu\text{-}L')\}2Co]$,[17] $[\{CoN(SiMe_3)_2(\mu\text{-}\eta\text{-}o\text{-}C6H_4(\kappa NSiiPr_3)_2)\}_2Co]$[54] and $[Co_3(pymp)_4(MeOH)_2](BPh_4)_2{\cdot}2MeOH$ (Hpymp = 2-[(pyridine-2-ylimine)-methyl]phenol).[129] When the magneto-structural data for **2′** are compared with those for these complexes one realises that all of them exhibit linear geometry, weak to medium magnetic exchange interactions between the Co^{II} ions (ferro-or antiferromagnetic) and easy-axis anisotropy of the local Co^{II} ions. Moreover, the SMM properties improve when the magnitude of the two latter features (magnetic coupling and easy-axis anisotropy) increases. Thus, complex **2′**, with stronger calculated easy-axis anisotropy of the local Co^{II} ions and a larger magnetic exchange coupling (J = −10.1 cm^{-1}) than the structurally related complex $[\{Co(\mu\text{-}L')\}_2Co]$ (J = −6.4 cm^{-1}), exhibits a higher effective energy barrier for magnetisation reversal, U_{eff}, than the latter (see above). In the case of $[Co_3(pymp)_4(MeOH)_2](BPh_4)_2{\cdot}2MeOH$, with only two phenoxido-bridges between the Co^{II} ions, the magnetic coupling (J = +4.8 cm^{-1} *vs.* J = −10.1 cm^{-1}) as well as the average easy-axis anisotropy of the local Co^{II} ions (D = −27 cm^{-1}) are rather smaller than in **2′** and $[\{Co(\mu\text{-}L')\}_2Co]$, and this is the reason why, despite observing out-of-phase ac signals around 2 K, they do not reach any maximum. It is worth noting that when MeOH is replaced with pyridine-2-amine in $[Co_3(pymp)_4(MeOH)_2](BPh_4)_2{\cdot}2MeOH$, the average D value remains almost constant but the magnetic coupling significantly decreases (J = 1.3 cm^{-1}) and no out-of-phase signals are observed above 2 K. Interestingly, the complex $[\{CoN(SiMe_3)_2(\mu\text{-}\eta\text{-}o\text{-}C_6H_4(\kappa NSiiPr_3)_2)\}_2Co]$, which contains three-coordinate terminal Co^{II} ions and a central Co^{II} ion "sandwiched" between the *o*-phenylenes of the two *o*-phenylene-*N*-alkyl-*N*′-(trialkylsilyl)amides ligands, presents a larger magnetic coupling value (J = +16.8 cm^{-1}) than **2′** and $[\{Co(\mu\text{-}L')\}_2Co]$. However, in $[\{CoN(SiMe_3)_2(\mu\text{-}\eta\text{-}o\text{-}C6H_4(\kappa NSiiPr_3)_2)\}_2Co]$, the easy-axis anisotropy of the local Co(II) ions is expected to be lower than in **1** and $[\{Co(\mu\text{-}L')\}_2Co]$. Moreover, the anisotropy axes are presumably not collinear, which could lead to a smaller anisotropy of the whole molecule. We believe that the effect of the large magnetic coupling is cancelled by the other two factors (magnetic anisotropy and

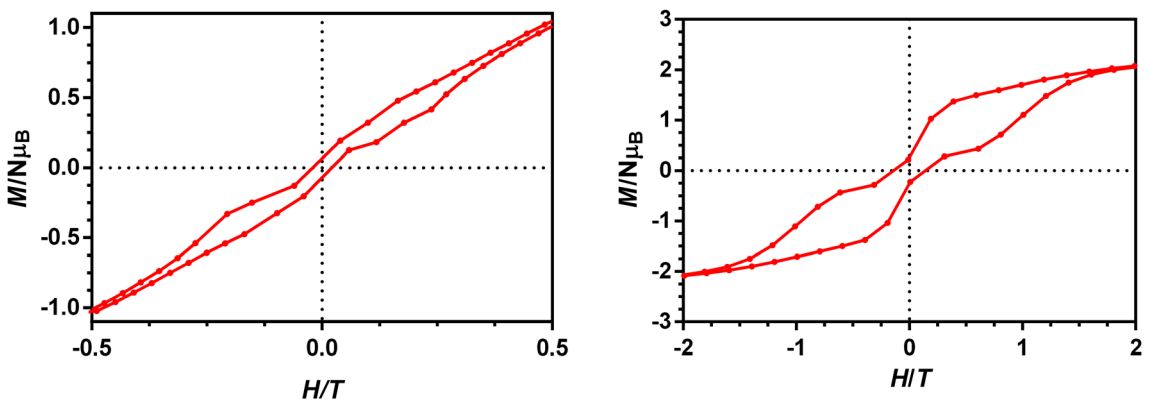

Fig. 10 Magnetic hysteresis loops for **1** (left) and **2** (right) at 2k with a 100 Oe s^{-1} sweep rate.

non-collinear anisotropic axes), so that the experimental U_{eff} for [{CoN(SiMe$_3$)$_2$(μ-η-*o*-C6H$_4$(κNSiiPr$_3$)$_2$)}$_2$Co] is similar to those found in **1** and [{Co(μ-L′)}$_2$Co].

Conclusions

We have prepared two new Schiff base tripodal pro-ligands, **L** and **H$_3$L1**, by reaction of the *cis*,*cis*-1,3,5-tiaminocyclohexane with either 1-methylimidazole-2-carbaldehyde or salicylaldehyde, respectively. The pro-ligands allowed the preparation of the mononuclear complex [Co^{II}L](ClO$_4$)$_2$ (**1**) and the trinuclear linear phenoxido-bridged complex [(Co^{II}L1)$_2$Co^{II}] (**2**). Compound **1** exhibits a CoN$_6$ coordination environment with a slightly compressed trigonal prismatic geometry and strict C_3 symmetry, where the C_3 passes along the barycentre of the cyclohexane ring. These facts support the hypothesis that the use of the 1-methylimidazole moiety in these kinds of tripodal ligands generally leads to complexes with C_3 symmetry. Because the C_3 symmetry requires the absence of rhombic anisotropy, E should be zero, and the ground state would present pure easy-axis magnetic anisotropy. Moreover, the parallel distribution of anisotropy axis in the structure improves the easy-axis magnetic anisotropy of the compound. The few examples of trigonal prismatic Co^{II} mononuclear complexes reported so far with C_3 symmetry possess $2D^*$ values (energy gap between the ground and first excited Kramers doublets) close to −225 cm^{-1}, which can be considered as the upper limit of easy-axis magnetic anisotropy for trigonal prismatic Co^{II} complexes. Owing to the strong and pure axial anisotropy of **1**, the absence of Co^{II}···Co^{II} intermolecular interactions and the parallel distribution of the anisotropy axes in the structure, QTM is quenched and this compound shows slow magnetic relaxation at zero applied magnetic field and open magnetic hysteresis at 2 K, which is rather unusual in Co^{II} mononuclear complexes. At zero field the magnetic relaxation essentially occurs through a combination of QTM and Raman processes, whereas in the presence of a small magnetic field the relaxation takes place only *via* a Raman relaxation process, which is rather usual for hexacoordinated Co^{II} complexes. On the other hand, the results reported for **2′** validate those previously reported for the trinuclear linear Co$_3$ complex [{Co(μ-L′)}2Co] (H$_3$L′ = Schiff base derived from the condensation of tris (methylhidrazido)phosphorylsulfide and salicylaldehyde). These findings confirm that, to present SMM behaviour and open hysteresis at zero dc magnetic field, a linear Co$_3$ trimer needs not only to have strong magnetic exchange interactions between the Co^{II} ions but also easy-axis magnetic anisotropy of each local Co^{II} ion. Collinearity of the anisotropy axes also contributes to increasing the anisotropy of the whole molecule, thus helping to improve the SMM properties. The magnetic relaxation takes place through an Orbach process *via* the first excited magnetic exchange KD.

Work is in progress in our lab directed towards: (i) the preparation of new Co$_3$ complexes similar to **2′**, incorporating either electron-donating or electron-withdrawing groups on the phenolic ring, and the study of the resulting electronic effects on the their SMM properties and (ii) the processing of mononuclear and trinuclear Co^{II} complexes with efficient SMM properties, like **1** and **2′**, on different types of SiO$_2$ nanoparticles and the analysis of how their SMM properties are modified.

Author contributions

L. C. C. synthesized and spectroscopically characterized the compounds. M. M. Q.-M. carried out the quantum-chemical calculations. E. R.-B. and J. M. G.-Z. solved the crystal structures of **2** and **2′** and recorded the corresponding X-ray powder diffraction diagrams. J. K. and M. O. performed the HFEPR and FIRMS studies J.-R. J. solved the crystal structure of **1** and directed the experimental work. E. C. conceived the idea and wrote the original draft. E. C. and J.-R. J. acquired the financial support. All authors discussed the results and commented and reviewed/edited the manuscript.

Conflicts of interest

There are no conflicts to declare

Data availability

The data supporting this article have been included as part of the supplementary information (SI). Supplementary information: crystallographic data, PXRD, magnetic plots and tables, and computational analysis plots and tables. See DOI: **https://doi.org/10.1039/d5qi02196k**.

CCDC 2497812–2497814 contain the supplementary crystallographic data for this paper.[130a–c]

Acknowledgements

Financial support from Ministerio de Ciencia e Innovación (Project PID2022-138090NB-C21 funded by MCIN/AEI/10.13039/501100011033/FEDER, UE), Consejería de Universidad, Investigación e Innovación and ERDF Andalusia Program 2021–2027 (projects C-EXP-140-UGR23 and M.1.B.B TA_000722_UJA23), Junta de Andalucía (FQM-195 and FQM-337), the University of Granada and the University of Jaén are gratefully acknowledged. The authors acknowledge the Centro de Servicios de Informática y Redes de Comunicaciones (CSIRC) for computational time and facilities. M. M. Q. M. and J. R. J. thank Ministerio de Ciencia e Innovación for their Ramón y Cajal contracts (RYC2021-034288-I and RYC2022-037255-I, respectively, funded both by MCIN/AEI/10.13039/501100011033 and by FSE+ and the European Union "NextGenerationEU"/PRTR", respectively). Part of this work was performed at the NHMFL, which is funded by the National Science Foundation (Cooperative

Agreement DMR 2128556) and the State of Florida. J. M. G.-Z. E. R. B. thank Ministerio de Ciencia e Innovación for financial support (PID2022-139530NB-I00).

References

1 D. Gatteschi and R. Sessoli, Quantum Tunneling of Magnetization and Related Phenomena in Molecular Materials, *Angew. Chem., Int. Ed.*, 2003, **42**, 268–297.
2 D. Gatteschi, R. Sessoli and J. Villain, *Molecular Nanomagnets*, Oxford University Press, Oxford, 2006.
3 J. Bartolomé, F. Luis and J. F. Fernández, *Molecular Magnets*, Springer-Verlag, Berlin-Heidelberg, 2014.
4 Y.-S. Meng, S.-D. Jiang, B.-W. Wang and S. Gao, Understanding the Magnetic Anisotropy toward Single-Ion Magnets, *Acc. Chem. Res.*, 2016, **49**, 2381–2389.
5 A. Dey, P. Kalita and V. Chandrasekhar, Lanthanide(III)-Based Single-Ion Magnets, *ACS Omega*, 2018, **3**, 9462–9475.
6 M. Feng and M. Tong, Single Ion Magnets from 3d to 5f: Developments and Strategies, *Chem. – Eur. J.*, 2018, **24**, 7574–7594.
7 A. Zabala-Lekuona, J. M. Seco and E. Colacio, Single-Molecule Magnets: From Mn12-ac to dysprosium metallocenes, a travel in time, *Coord. Chem. Rev.*, 2021, **441**, 213984.
8 N. F. Chilton, Molecular Magnetism, *Annu. Rev. Mater. Res.*, 2022, **52**, 79–101.
9 X. Yin, L. Deng, L. Ruan, Y. Wu, F. Luo, G. Qin, X. Han and X. Zhang, Recent Progress for Single-Molecule Magnets Based on Rare Earth Elements, *Materials*, 2023, **16**, 3568.
10 E. Moreno-Pineda and W. Wernsdorfer, Magnetic Molecules as Building Blocks for Quantum Technologies, *Adv. Quantum Technol.*, 2024, **8**, 2300367.
11 G. Taran, E. Bonet and W. Wernsdorfer, in *Handbook of Magnetism and Magnetic Materials*, ed. J. M. D. Coey and S. S. P. Parkin, Springer International Publishing, Cham, 2021, pp. 979–1009.
12 L. Bogani and W. Wernsdorfer, Molecular spintronics using single-molecule magnets, *Nat. Mater.*, 2008, **7**, 179–186.
13 D. Gatteschi, A. Cornia, M. Mannini and R. Sessoli, Organizing and Addressing Magnetic Molecules, *Inorg. Chem.*, 2009, **48**, 3408–3419.
14 R. Vincent, S. Klyatskaya, M. Ruben, W. Wernsdorfer and F. Balestro, Electronic read-out of a single nuclear spin using a molecular spin transistor, *Nature*, 2012, **488**, 357–360.
15 E. Coronado, Molecular magnetism: from chemical design to spin control in molecules, materials and devices, *Nat. Rev. Mater.*, 2019, **5**, 87–104.
16 E. Moreno-Pineda and W. Wernsdorfer, Measuring molecular magnets for quantum technologies, *Nat. Rev. Phys.*, 2021, **3**, 645–659.
17 B. R. Sankhi, E. Peigney, H. Brown, P. Suh, C. Rojas-Dotti, J. Martínez-Lillo and P. Tyagi, Single-molecule Magnets (SMM) spin channels connecting FeMn antiferromagnet and NiFe ferromagnetic electrodes of a tunnel junction, *J. Magn. Magn. Mater.*, 2024, **611**, 172608.
18 J. D. Rinehart and J. R. Long, Exploiting single-ion anisotropy in the design of f-element single-molecule magnets, *Chem. Sci.*, 2011, **2**, 2078.
19 J.-L. Liu, Y.-C. Chen and M.-L. Tong, Symmetry strategies for high performance lanthanide-based single-molecule magnets, *Chem. Soc. Rev.*, 2018, **47**, 2431–2453.
20 Y.-S. Meng, S.-D. Jiang, B.-W. Wang and S. Gao, Understanding the Magnetic Anisotropy toward Single-Ion Magnets, *Acc. Chem. Res.*, 2016, **49**, 2381–2389.
21 L. Ungur and L. F. Chibotaru, Strategies toward High-Temperature Lanthanide-Based Single-Molecule Magnets, *Inorg. Chem.*, 2016, **55**, 10043–10056.
22 C. A. P. Goodwin, F. Ortu, D. Reta, N. F. Chilton and D. P. Mills, Molecular magnetic hysteresis at 60 kelvin in dysprosocenium, *Nature*, 2017, **548**, 439–442.
23 F.-S. Guo, B. M. Day, Y.-C. Chen, M.-L. Tong, A. Mansikkamäki and R. A. Layfield, Magnetic hysteresis up to 80 kelvin in a dysprosium metallocene single-molecule magnet, *Science*, 2018, **362**, 1400–1403.
24 J. Emerson-King, G. K. Gransbury, B. E. Atkinson, W. J. A. Blackmore, G. F. S. Whitehead, N. F. Chilton and D. P. Mills, Soft magnetic hysteresis in a dysprosium amide–alkene complex up to 100 kelvin, *Nature*, 2025, **643**, 125–129.
25 P. C. Bunting, M. Atanasov, E. Damgaard-Møller, M. Perfetti, I. Crassee, M. Orlita, J. Overgaard, J. van Slageren, F. Neese and J. R. Long, A linear cobalt(II) complex with maximal orbital angular momentum from a non-Aufbau ground state, *Science*, 2018, **362**, eaat7319.
26 Y. Gil, M. M. Quesada-Moreno, M. A. Palacios, S. Gómez-Coca, E. Colacio, E. Ruiz and D. Aravena, Determining the zero-field cooling/field cooling blocking temperature from AC susceptibility data for single-molecule magnets, *Inorg. Chem. Front.*, 2025, **12**, 2856–2871.
27 S. Dey, T. Sharma and G. Rajaraman, Unravelling the role of spin–vibrational coupling in designing high-performance pentagonal bipyramidal Dy(III) single ion magnets, *Chem. Sci.*, 2024, **15**, 6465–6477.
28 V. Vieru, S. Gómez-Coca, E. Ruiz and L. F. Chibotaru, Increasing the Magnetic Blocking Temperature of Single-Molecule Magnets, *Angew. Chem., Int. Ed.*, 2024, **63**, e202303146.
29 J. Wang, C. Sun, Q. Zheng, D. Wang, Y. Chen, J. Ju, T. Sun, Y. Cui, Y. Ding and Y. Tang, Magnetic relaxation in dysprosium complexes tuned by coordination geometry and counter anions, *Chem. – Asian J.*, 2023, **18**, e202201297.
30 Z. Zhu, M. Guo, X.-L. Li and J. Tang, Molecular magnetism of lanthanide: Advances and perspectives, *Coord. Chem. Rev.*, 2019, **378**, 350–364.
31 G. A. Craig and M. Murrie, 3d single-ion magnets, *Chem. Soc. Rev.*, 2015, **44**, 2135–2147.

32 J. M. Frost, K. L. M. Harriman and M. Murugesu, The rise of 3-d single-ion magnets in molecular magnetism: towards materials from molecules?, *Chem. Sci.*, 2016, **7**, 2470–2491.
33 S. Tripathi, A. Dey, M. Shanmugam, R. S. Narayanan and V. Chandrasekhar, Cobalt(II) complexes as single-ion magnets, in *Organometallic Magnets*, 2018, pp. 35–75.
34 Z. Zhu and J. Tang, Lanthanide single-molecule magnets with high anisotropy barrier: where to from here?, *Natl. Sci. Rev.*, 2022, **9**, nwac194.
35 Z. Zhu, C. Zhao, T. Feng, X. Liu, X. Ying, X.-L. Li, Y.-Q. Zhang and J. Tang, Air-Stable Chiral Single-Molecule Magnets with Record Anisotropy Barrier Exceeding 1800 K, *J. Am. Chem. Soc.*, 2021, **143**, 10077–10082.
36 Z. Zhu, S. Paul, C. Zhao, J. Wu, X. Ying, L. Ungur, W. Wernsdorfer, F. Meyer and J. Tang, Record Quantum Tunneling Time in an Air-Stable Exchange-Bias Dysprosium Macrocycle, *J. Am. Chem. Soc.*, 2024, **146**, 18899–18904.
37 Z. Zhu, T. Wang, L. A. Mariano, S. Paul, W. Wernsdorfer, A. Lunghi and J. Tang, Chiral Dysprosium-[7]Helicene Macrocycles Showing Record Single-Molecule Magnet Properties in the Lanthanide–Helicene Family, *J. Am. Chem. Soc.*, 2025, **147**, 42815–42824.
38 A. Sarkar, S. Dey and G. Rajaraman, Magnetic anisotropy in FeII, CoII and NiII complexes: an ab initio perspective, *Chem. – Eur. J.*, 2020, **26**, 14036–14058.
39 J. Juráková and I. Šalitroš, Co(II) single-ion magnets: synthesis, structure, and magnetic properties, *Monatsh. Chem.*, 2022, **153**, 1001–1036.
40 P. K. Sahu, R. Kharel, S. Shome, S. Goswami and S. Konar, Understanding the unceasing evolution of Co(II) based single-ion magnets, *Coord. Chem. Rev.*, 2023, **475**, 214871.
41 M. Wang, Z. Han, Y. Garcia and P. Cheng, Six-Coordinated CoII Single-Molecule Magnets: Synthetic Strategy, Structure and Magnetic Properties, *ChemPhysChem*, 2024, **25**, e202400396.
42 A. A. Pavlov, D. Y. Aleshin, S. A. Savkina, A. S. Belov, N. N. Efimov, J. Nehrkorn, M. Ozerov, Y. Z. Voloshin, Y. V. Nelyubina and V. V. Novikov, New Spin-Crossover Complexes of Substituted 2,6-Bis(pyrazol-3-yl)pyridines, *ChemPhysChem*, 2019, **20**, 1001–1005.
43 A. A. Pavlov, Y. V. Nelyubina, S. V. Kats, L. V. Penkova, N. N. Efimov, A. O. Dmitrienko, A. V. Vologzhanina, A. S. Belov, Y. Z. Voloshin and V. V. Novikov, Very Large Magnetic Anisotropy of Cage Cobalt(II) Complexes with a Rigid Cholesteryl Substituent from Paramagnetic NMR Spectroscopy, *J. Phys. Chem. Lett.*, 2016, **7**, 4111–4116.
44 A. Landart-Gereka, M. M. Quesada-Moreno, M. A. Palacios, I. F. Díaz-Ortega, H. Nojiri, M. Ozerov, J. Krzystek and E. Colacio, Pushing up the easy-axis magnetic anisotropy and relaxation times in trigonal prismatic CoII mononuclear SMMs by molecular structure design, *Chem. Commun.*, 2023, **59**, 952–955.
45 A. Landart-Gereka, M. M. Quesada-Moreno, I. F. Díaz-Ortega, H. Nojiri, M. Ozerov, J. Krzystek, M. A. Palacios and E. Colacio, Large easy-axis magnetic anisotropy in a series of trigonal prismatic mononuclear cobalt(II) complexes with zero-field hidden single-molecule magnet behaviour: the important role of the distortion of the coordination sphere and intermolecular interactions in the slow relaxation, *Inorg. Chem. Front.*, 2022, **9**, 2810–2831.
46 Y. P. Tupolova, V. E. Lebedev and I. N. Shcherbakov, Can the continuous symmetry measure TPR6 measure the axial magnetic anisotropy in hexacoordinated Co(II) SIMs?, *New J. Chem.*, 2023, **47**, 10484–10487.
47 Y. Peng, T. Bodenstein, K. Fink, V. Mereacre, C. E. Anson and A. K. Powell, Magnetic anisotropy of a CoII single ion magnet with distorted trigonal prismatic coordination: theory and experiment, *Phys. Chem. Chem. Phys.*, 2016, **18**, 30135–30143.
48 A. Landart, M. M. Quesada-Moreno, M. A. Palacios, Y. Li, M. Ozerov, J. Krzystek and E. Colacio, Control of the geometry and anisotropy driven by the combination of steric and anion coordination effects in CoII complexes with N6-tripodal ligands: the impact of the size of the ligand on the magnetization relaxation time, *Dalton Trans.*, 2024, **53**, 12876–12892.
49 M. A. Palacios, J. Nehrkorn, E. A. Suturina, E. Ruiz, S. Gómez-Coca, K. Holldack, A. Schnegg, J. Krzystek, J. M. Moreno and E. Colacio, Analysis of Magnetic Anisotropy and the Role of Magnetic Dilution in Triggering Single-Molecule Magnet (SMM) Behavior in a Family of CoIIYIII Dinuclear Complexes with Easy-Plane Anisotropy, *Chem. – Eur. J.*, 2017, **23**, 11649–11661.
50 F. Pointillart, K. Bernot, S. Golhen, B. Le Guennic, T. Guizouarn, L. Ouahab and O. Cador, Magnetic Memory in an Isotopically Enriched and Magnetically Isolated Mononuclear Dysprosium Complex, *Angew. Chem., Int. Ed.*, 2015, **54**, 1504–1507.
51 J. Flores-Gonzalez, F. Pointillart and O. Cador, Hyperfine coupling and slow magnetic relaxation in isotopically enriched DyIII mononuclear single-molecule magnets, *Inorg. Chem. Front.*, 2019, **6**, 1081–1086.
52 A. Lunghi and S. Sanvito, Multiple spin-phonon relaxation pathways in a Kramer single-ion magnet, *J. Chem. Phys.*, 2020, **153**, 174113.
53 R. Nabi, B. E. Atkinson, J. K. Staab, J. M. Skelton and N. F. Chilton, The impact of low-energy phonon lifetimes on the magnetic relaxation in a dysprosocenium single-molecule magnet, *Chem. Commun.*, 2024, **60**, 13915–13918.
54 M. Briganti, F. Santanni, L. Tesi, F. Totti, R. Sessoli and A. Lunghi, A Complete *Ab Initio* View of Orbach and Raman Spin–Lattice Relaxation in a Dysprosium Coordination Compound, *J. Am. Chem. Soc.*, 2021, **143**, 13633–13645.
55 J. M. Zadrozny, M. Atanasov, A. M. Bryan, C.-Y. Lin, B. D. Rekken, P. P. Power, F. Neese and J. R. Long, Slow magnetization dynamics in a series of two-coordinate iron (II) complexes, *Chem. Sci.*, 2013, **4**, 125–138.

56 D. H. Moseley, S. E. Stavretis, K. Thirunavukkuarasu, M. Ozerov, Y. Cheng, L. L. Daemen, J. Ludwig, Z. Lu, D. Smirnov, C. M. Brown, A. Pandey, A. J. Ramirez-Cuesta, A. C. Lamb, M. Atanasov, E. Bill, F. Neese and Z.-L. Xue, Spin–phonon couplings in transition metal complexes with slow magnetic relaxation, *Nat. Commun.*, 2018, **9**, 2572.

57 S. Nain, M. Kumar and M. E. Ali, The impact of spin-vibrational coupling on magnetic relaxation of a Co(II) single-molecule magnet, *Phys. Chem. Chem. Phys.*, 2023, **25**, 14848–14861.

58 A. Castro-Alvarez, Y. Gil, L. Llanos and D. Aravena, High performance single-molecule magnets, Orbach or Raman relaxation suppression?, *Inorg. Chem. Front.*, 2020, **7**, 2478–2486.

59 A. Lunghi, F. Totti, S. Sanvito and R. Sessoli, Intra-molecular origin of the spin-phonon coupling in slow-relaxing molecular magnets, *Chem. Sci.*, 2017, **8**, 6051–6059.

60 S. K. Langley, D. P. Wielechowski, V. Vieru, N. F. Chilton, B. Moubaraki, B. F. Abrahams, L. F. Chibotaru and K. S. Murray, A {$CrIII_2$ $DyIII_2$} Single–Molecule Magnet: Enhancing the Blocking Temperature through 3d Magnetic Exchange, *Angew. Chem., Int. Ed.*, 2013, **52**, 12014–12019.

61 K. R. Vignesh, S. K. Langley, K. S. Murray and G. Rajaraman, Quenching the Quantum Tunneling of Magnetization in Heterometallic Octanuclear {$TMIII_4$ $DyIII_4$} (TM=Co and Cr) Single–Molecule Magnets by Modification of the Bridging Ligands and Enhancing the Magnetic Exchange Coupling, *Chem. – Eur. J.*, 2017, **23**, 1654–1666.

62 X.-L. Li, F.-Y. Min, C. Wang, S.-Y. Lin, Z. Liu and J. Tang, Utilizing 3d–4f Magnetic Interaction to Slow the Magnetic Relaxation of Heterometallic Complexes, *Inorg. Chem.*, 2015, **54**, 4337–4344.

63 J. Li, R.-M. Wei, T.-C. Pu, F. Cao, L. Yang, Y. Han, Y.-Q. Zhang, J.-L. Zuo and Y. Song, Tuning quantum tunnelling of magnetization through 3d–4f magnetic interactions: an alternative approach for manipulating single-molecule magnetism, *Inorg. Chem. Front.*, 2017, **4**, 114–122.

64 Y. Peng, M. K. Singh, V. Mereacre, C. E. Anson, G. Rajaraman and A. K. Powell, Mechanism of magnetisation relaxation in {$MIII_2DyIII_2$} (M = Cr, Mn, Fe, Al) "Butterfly" complexes: how important are the transition metal ions here?, *Chem. Sci.*, 2019, **10**, 5528–5538.

65 J.-P. Costes, G. Novitchi, V. Vieru, L. F. Chibotaru, C. Duhayon, L. Vendier, J.-P. Majoral and W. Wernsdorfer, Effects of the Exchange Coupling on Dynamic Properties in a Series of CoGdCo Complexes, *Inorg. Chem.*, 2019, **58**, 756–768.

66 L. Ungur, M. Thewissen, J.-P. Costes, W. Wernsdorfer and L. F. Chibotaru, Interplay of strongly anisotropic metal ions in magnetic blocking of complexes, *Inorg. Chem.*, 2013, **52**, 6328–6337.

67 M. N. Akhtar, M. A. AlDamen, C. D. McMillen, A. Escuer and J. Mayans, Exploring the Role of Intramolecular Interactions in the Suppression of Quantum Tunneling of the Magnetization in a 3d-4f Single-Molecule Magnet, *Inorg. Chem.*, 2021, **60**, 9302–9308.

68 Y.-N. Guo, G.-F. Xu, W. Wernsdorfer, L. Ungur, Y. Guo, J. Tang, H.-J. Zhang, L. F. Chibotaru and A. K. Powell, Strong axiality and Ising exchange interaction suppress zero-field tunneling of magnetization of an asymmetric Dy_2 single-molecule magnet, *J. Am. Chem. Soc.*, 2011, **133**, 11948–11951.

69 J. D. Rinehart, M. Fang, W. J. Evans and J. R. Long, Strong exchange and magnetic blocking in N_2^{3-}-radical-bridged lanthanide complexes, *Nat. Chem.*, 2011, **3**, 538–542.

70 S. Demir, M. I. Gonzalez, L. E. Darago, W. J. Evans and J. R. Long, Giant coercivity and high magnetic blocking temperatures for N_2^{3-} radical-bridged dilanthanide complexes upon ligand dissociation, *Nat. Commun.*, 2017, **8**, 2144.

71 J. J. Le Roy, L. Ungur, I. Korobkov, L. F. Chibotaru and M. Murugesu, Coupling Strategies to Enhance Single-Molecule Magnet Properties of Erbium–Cyclooctatetraenyl Complexes, *J. Am. Chem. Soc.*, 2014, **136**, 8003–8010.

72 T. P. Latendresse, N. S. Bhuvanesh and M. Nippe, Hard Single-Molecule Magnet Behavior by a Linear Trinuclear Lanthanide-[1]Metallocenophane Complex, *J. Am. Chem. Soc.*, 2017, **139**, 14877–14880.

73 C. A. Gould, K. R. McClain, D. Reta, J. G. C. Kragskow, D. A. Marchiori, E. Lachman, E.-S. Choi, J. G. Analytis, R. D. Britt, N. F. Chilton, B. G. Harvey and J. R. Long, Ultrahard magnetism from mixed-valence dilanthanide complexes with metal-metal bonding, *Science*, 2022, **375**, 198–202.

74 U. Albold, H. Bamberger, P. P. Hallmen, J. van Slageren and B. Sarkar, Strong Exchange Couplings Drastically Slow Down Magnetization Relaxation in an Air-Stable Cobalt(II)-Radical Single-Molecule Magnet (SMM), *Angew. Chem., Int. Ed.*, 2019, **58**, 9802–9806.

75 A. Zabala-Lekuona, A. Landart-Gereka, M. M. Quesada-Moreno, A. J. Mota, I. F. Díaz-Ortega, H. Nojiri, J. Krzystek, J. M. Seco and E. Colacio, Zero-Field SMM Behavior Triggered by Magnetic Exchange Interactions and a Collinear Arrangement of Local Anisotropy Axes in a Linear Co_3II Complex, *Inorg. Chem.*, 2023, **62**, 20030–20041.

76 T. Bowen, R. P. Planalp and M. W. Brechbiel, Synthesis of novel hexadentate ligand derivatives for the preparation of gallium radiopharmaceuticals, *Bioorg. Med. Chem. Lett.*, 1996, **6**, 807–810.

77 D. Ben-Ishai and A. Berger, Cleavage of N-carbobenzoxy groups by dry hydrogen bromide and hydrogen chloride, *J. Org. Chem.*, 1952, **17**, 1564–1570.

78 J. Nehrkorn, J. Telser, K. Holldack, S. Stoll and A. Schnegg, Simulating Frequency-Domain Electron Paramagnetic Resonance: Bridging the Gap between Experiment and Magnetic Parameters for High-Spin Transition-Metal Ion Complexes, *J. Phys. Chem. B*, 2015, **119**, 13816–13824.

79 S. Stoll and A. Schweiger, EasySpin, a comprehensive software package for spectral simulation and analysis in EPR, *J. Magn. Reson.*, 2006, **178**, 42–55.
80 A. K. Hassan, L. A. Pardi, J. Krzystek, A. Sienkiewicz, P. Goy, M. Rohrer and L.-C. Brunel, Ultrawide band multifrequency high-field EMR technique: A methodology for increasing spectroscopic information, *J. Magn. Reson.*, 2000, **142**, 300–312.
81 *APEX2, Version 2010*, Bruker AXS Inc., Madison, WI, 2010.
82 *SAINT, Version 8.30a*, Bruker AXS Inc., Madison, WI, 2013.
83 G. M. Sheldrick, *SADABS, Version 2008*, Bruker AXS Inc., Madison, WI, 2008.
84 *CrysAlisPro Software System, Version 2012*, Agilent Technologies UK Ltd, Oxford, UK, 2012.
85 G. M. Sheldrick, SHELXT – Integrated space-group and crystal-structure determination, *Acta Crystallogr., Sect. A: Found. Adv.*, 2015, **71**, 3–8.
86 G. M. Sheldrick, SHELXL – Integrated space-group and crystal-structure refinement, *Acta Crystallogr., Sect. C: Struct. Chem.*, 2015, **71**, 3–8.
87 O. V. Dolomanov, L. J. Bourhis, R. J. Gildea, J. A. K. Howard and H. Puschmann, OLEX2: a complete structure solution, refinement and analysis program, *J. Appl. Crystallogr.*, 2009, **42**, 339–341.
88 P.-Å. Malmqvist and B. O. Roos, The CASSCF state interaction method, *Chem. Phys. Lett.*, 1989, **155**, 189–194.
89 C. Angeli, R. Cimiraglia and J.-P. Malrieu, N-electron valence state perturbation theory: A fast implementation of the strongly contracted variant, *Chem. Phys. Lett.*, 2001, **350**, 297–305.
90 C. Angeli, R. Cimiraglia, S. Evangelisti, T. Leininger and J.-P. Malrieu, Introduction of *n*-electron valence states for multireference perturbation theory, *J. Chem. Phys.*, 2001, **114**, 10252–10264.
91 C. Angeli, R. Cimiraglia and J.-P. Malrieu, *N*-electron valence state perturbation theory: A spinless formulation and an efficient implementation of the strongly contracted and of the partially contracted variants, *J. Chem. Phys.*, 2002, **117**, 9138–9153.
92 F. Weigend and R. Ahlrichs, Balanced basis sets of split valence, triple zeta valence and quadruple zeta valence quality for H to Rn: Design and assessment of accuracy, *Phys. Chem. Chem. Phys.*, 2005, **7**, 3297.
93 A. Schäfer, H. Horn and R. Ahlrichs, Fully optimized contracted Gaussian basis sets for atoms Li to Kr, *J. Chem. Phys.*, 1992, **97**, 2571–2577.
94 A. Schäfer, C. Huber and R. Ahlrichs, Fully optimized contracted Gaussian basis sets of triple zeta valence quality for atoms Li to Kr, *J. Chem. Phys.*, 1994, **100**, 5829–5835.
95 F. Neese, Software update: the ORCA program system—version 5.0, *Wiley Interdiscip. Rev.: Comput. Mol. Sci.*, 2022, **12**, e1606.
96 D. Ganyushin and F. Neese, A fully variational spin-orbit coupled complete active space self-consistent field approach: Application to electron paramagnetic resonance g-tensors, *J. Chem. Phys.*, 2013, **138**, 104113.
97 D. Ganyushin and F. Neese, First-principles calculations of zero-field splitting parameters, *J. Chem. Phys.*, 2006, **125**, 024103.
98 R. Maurice, R. Bastardis, C. de Graaf, N. Suaud, T. Mallah and N. Guihéry, Universal Theoretical Approach to Extract Anisotropic Spin Hamiltonians, *J. Chem. Theory Comput.*, 2009, **5**, 2977–2984.
99 F. Neese, Efficient and accurate approximations to the molecular spin–orbit coupling operator and their use in molecular g-tensor calculations, *J. Chem. Phys.*, 2005, **122**, 034107.
100 T. Nakajima and K. Hirao, The Douglas–Kroll–Hess Approach, *Chem. Rev.*, 2012, **112**, 385–402.
101 J. Jung, M. Atanasov and F. Neese, Ab Initio Ligand-Field Theory Analysis and Covalency Trends in Actinide and Lanthanide Free Ions and Octahedral Complexes, *Inorg. Chem.*, 2017, **56**, 8802–8816.
102 T. J. Ozumerzifon, I. Bhowmick, W. C. Spaller, A. K. Rappé and M. P. Shores, Toward steric control of guest binding modality: a cationic Co(II) complex exhibiting cation binding and zero-field relaxation, *Chem. Commun.*, 2017, **53**, 4211–4214.
103 C. M. Klug, T. J. Ozumerzifon, I. Bhowmick, B. N. Livesay, A. K. Rappé and M. P. Shores, Anionic guest-dependent slow magnetic relaxation in Co(II) tripodal iminopyridine complexes, *Dalton Trans.*, 2019, **48**, 9117–9126.
104 R. A. D. Wentworth, P. S. Dahl, C. J. Huffman, W. O. Gillum, W. E. Streib and J. C. Huffman, Hindered-ligand systems. 9. Structure of the cis,cis-1,3,5-tris(pyridine-2-carboxaldimino)cyclohexane complexes of cobalt (II) and zinc(II) ions, *Inorg. Chem.*, 1982, **21**, 3060–3063.
105 M. Llunell, D. Casanova, J. Cirera, P. Alemany and S. Alvarez, *SHAPE, Version 2.1*, University of Barcelona, Barcelona, Spain, 2013.
106 M. A. Palacios, M. M. Quesada-Moreno, S. F. Alrebei, C. Cuesta, E. Colacio and A. J. Mota, Magneto-Structural Correlations, Substitution Effects and Slow Relaxation of the Magnetization on Trinuclear Linear Ni(II) Complexes: An Experimental and Theoretical Study, *Chem. – Asian J.*, 2025, **20**(9), e202401565.
107 V. Chandrasekhar, R. Azhakar, G. T. S. Andavan, V. Krishnan, S. Zacchini, J. F. Bickley, A. Steiner, R. J. Butcher and P. Kögerler, A phosphorus supported multisite coordinating tris hydrazone P(S)[N(Me)N=CH-C_6H_4-o-OH]$_3$ as an efficient ligand for the assembly of trinuclear metal complexes: synthesis, structure, and magnetism, *Inorg. Chem.*, 2003, **42**, 5989–5998.
108 N. F. Chilton, R. P. Anderson, L. D. Turner, A. Soncini and K. S. Murray, PHI: a powerful new program for the analysis of anisotropic monomeric and exchange-coupled polynuclear d- and f-block complexes, *J. Comput. Chem.*, 2013, **34**, 1164–1175.
109 B. N. Figgis and M. A. Hitchman, *Ligand field theory and its applications*, Wiley-VCH, 2000.
110 F. Lloret, M. Julve, J. Cano, R. Ruiz-García and E. Pardo, Magnetic properties of six-coordinated high-spin cobalt

(II) complexes: Theoretical background and its application, *Inorg. Chim. Acta*, 2008, **361**, 3432–3445.

111 H. Sakiyama, Development of MagSaki Software for Magnetic Analysis of Dinuclear High-spin Cobalt(II) Complexes in an Axially Distorted Octahedral Field, *J. Chem. Software*, 2001, **7**, 171–177.

112 X. Song and X. Xue, Study on the Magneto-Structural Correlation of a New Dinuclear Cobalt(II) Complex with Double μ-Phenoxo Bridges, *ACS Omega*, 2020, **5**, 8347–8354.

113 Y.-Z. Zhang, A. J. Brown, Y.-S. Meng, H.-L. Sun and S. Gao, Linear trinuclear cobalt(II) single molecule magnet, *Dalton Trans.*, 2015, **44**, 2865–2870.

114 L. F. Chibotaru and L. Ungur, *SINGLE_ANISO*, KU Leuven, Leuven, Belgium, 2006.

115 L. F. Chibotaru and L. Ungur, Ab initio calculation of anisotropic magnetic properties of complexes. I. Unique definition of pseudospin Hamiltonians and their derivation, *J. Chem. Phys.*, 2012, **137**, 064112.

116 S. Gómez-Coca, D. Aravena, R. Morales and E. Ruiz, Large magnetic anisotropy in mononuclear metal complexes, *Coord. Chem. Rev.*, 2015, **289–290**, 379–392.

117 S. Sottini, G. Poneti, S. Ciattini, N. Levesanos, E. Ferentinos, J. Krzystek, L. Sorace and P. Kyritsis, *Inorg. Chem.*, 2016, **55**, 9537–9548.

118 J. R. Pilbrow, Effective g values for S = 3/2 and S = 5/2, *J. Magn. Reson.*, 1978, **31**, 479–490.

119 E. A. Suturina, D. Maganas, E. Bill, M. Atanasov and F. Neese, Magneto-Structural Correlations in a Series of Pseudotetrahedral $[CoII(XR)_4]^{2-}$ Single Molecule Magnets: An ab Initio Ligand Field Study, *Inorg. Chem.*, 2015, **54**, 9948–9961.

120 L. Ungur and L. F. Chibotaru, *POLY_ANISO*, KU Leuven, Leuven, Belgium, 2007.

121 T. J. Woods, M. F. Ballesteros-Rivas, S. Gómez-Coca, E. Ruiz and K. R. Dunbar, Relaxation Dynamics of Identical Trigonal Bipyramidal Cobalt Molecules with Different Local Symmetries and Packing Arrangements: Magnetostructural Correlations and ab inito Calculations, *J. Am. Chem. Soc.*, 2016, **138**, 16407–16416.

122 J. Zhang, J. Li, L. Yang, C. Yuan, Y.-Q. Zhang and Y. Song, Magnetic Anisotropy from Trigonal Prismatic to Trigonal Antiprismatic Co(II) Complexes: Experimental Observation and Theoretical Prediction, *Inorg. Chem.*, 2018, **57**, 3903–3912.

123 Y.-Z. Zhang, S. Gómez-Coca, A. J. Brown, M. R. Saber, X. Zhang and K. R. Dunbar, Trigonal antiprismatic Co(II) single molecule magnets with large uniaxial anisotropies: importance of Raman and tunneling mechanisms, *Chem. Sci.*, 2016, **7**, 6519–6527.

124 F. S. Santana, M. Perfetti, M. Briganti, F. Sacco, G. Poneti, E. Ravera, J. F. Soares and R. Sessoli, A dysprosium single molecule magnet outperforming current pseudocontact shift agents, *Chem. Sci.*, 2022, **13**, 5860–5871.

125 A. Abragam and B. Bleaney, *Electron paramagnetic resonance of transition ions*, Oxford University Press, 2012.

126 A. Singh and K. N. Shrivastava, Optical–acoustic two-phonon relaxation in spin systems, *Phys. Status Solidi B*, 1979, **95**, 273–277.

127 K. N. Shrivastava, Theory of spin–lattice relaxation, *Phys. Status Solidi B*, 1983, **117**, 437–458.

128 M. E. Lines, Orbital angular momentum in the theory of paramagnetic clusters, *J. Chem. Phys.*, 1971, **55**, 2977–2984.

129 K. Y. Monakhov, J. van Leusen, P. Kögerler, E. Zins, M. E. Alikhani, M. Tromp, A. A. Danopoulos and P. Braunstein, Linear, Trinuclear Cobalt Complexes with o-Phenylene-bis-Silylamido Ligands, *Chem. – Eur. J.*, 2017, **23**, 6504–6508.

130 (*a*) CCDC 2497812: Experimental Crystal Structure Determination, 2026, DOI: **10.5517/ccdc.csd.cc2pv5lb**; (*b*) CCDC 2497813: Experimental Crystal Structure Determination, 2026, DOI: **10.5517/ccdc.csd.cc2pv5mc**; (*c*) CCDC 2497814: Experimental Crystal Structure Determination, 2026, DOI: **10.5517/ccdc.csd.cc2pv5nd**.

